

Bachelor Thesis

Orbital Doppler Boosting in supermassive black hole binaries

Kilian Fischer

Würzburg, 5th May, 2024



Julius-Maximilians-Universität Würzburg

Faculty of Physics and Astronomy

Chair for Astronomy

Supervisor: Prof. Sara Buson

Abstract

Active galactic nuclei (AGN) often show variability in their luminosity. With increasing observation time, periodic patterns emerge and are better distinguished from stochastic processes. It is suggested that supermassive black hole binaries (SMBHBs) in the centre of AGN lead to such periodic variabilities. In D’Orazio and Charisi (2023) [1] several signatures of SMBHBs are described. In this work, we will focus on the effect of orbital Doppler boosting, in which the emission from one of the supermassive black holes (SMBHs) gets Doppler boosted, and thus, appears brighter and bluer (or dimmer and redder) when the SMBH moves towards (or away from) the observer. A previous study on orbital Doppler boosting has been performed in D’Orazio and Charisi (2023) [1] with observation data in the optical and the ultraviolet wavebands. In this thesis, we will test a sample using the observations in gamma ray from *Fermi*-LAT regarding the question of whether or not the variability can be explained by orbital Doppler boosting. For that, we performed a *Fermi* analysis of the sources of this sample and plotted their light curve. To cope with the macro-trend in the light curve the Spline detrending was applied before the amplitude was extracted through a sine fit onto the data points. To get the optimal detrending, the Spline method was further improved and a method was developed to determine the best Spline binning. After the light curve was detrended, a sinusoidal wave function was fitted onto the data points. With this sine fit, the amplitude of the variability was determined and then used in the evaluation of the Doppler-boost hypothesis. As a result of this analysis, it was shown that the variability observed in PG 1553+113 and in PKS 2155-304 can be explained by orbital Doppler boosting of the jet emission from the smaller SMBH. Furthermore, for PG 1553+113 it is even possible that the variability originates from the jet of the more massive SMBH. For the other three sources PKS 0454-234, S5 0716+714 and OJ 014 the Doppler-boost hypothesis is not viable. For future works, we suggest a more generalised Doppler equation that also accounts for the Doppler boosting of two jets and a multi-wavelength study.

Zusammenfassung

Aktive Galaxienkerne (AGN) kennzeichnen sich durch eine sehr hohe bolometrische Helligkeit, die die Leuchtkraft der umgebenden Galaxie bei Weitem übersteigt. AGN weisen häufig Schwankungen in ihrer Helligkeit auf, insbesondere die Untergruppe der Blazare, deren Jet zu uns gerichtet ist. Mit zunehmender Beobachtungszeit lassen sich die periodischen Muster besser von den zufälligen Prozessen unterscheiden. Es wird vermutet, dass ein Binärsystem von zwei supermassereichen Schwarzen Löchern (SMBHB) im Zentrum von AGN zu solchen periodischen Variabilitäten führt. In D’Orazio und Charisi (2023) [1] werden mehrere Anzeichen von Binärsystemen im Zentrum der AGN beschrieben. In dieser Arbeit werden wir uns auf den Effekt der orbitalen Dopplerverstärkung konzentrieren, bei der die Jet Emission eines der supermassereichen Schwarzen Löcher (SMBHs) dopplerverstärkt wird. Eine frühere Studie zur orbitalen Dopplerverstärkung wurde in D’Orazio und Charisi (2023) [1] mit Beobachtungsdaten im optischen und ultravioletten Wellenbereich durchgeführt. In dieser Arbeit werden wir anhand der Beobachtungsdaten von *Fermi* im Gamma Bereich (MeV bis GeV) für fünf vielversprechende Quellen die Dopplereffektthese testen und auf eine mögliche Erklärung der Variabilität mittels Dopplerverstärkung eingehen. Zu diesem Zweck haben wir für jede Quelle eine *Fermi*-Analyse durchgeführt und ihre Lichtkurve ermittelt. Zur Bereinigung des Langzeittrends in den Lichtkurven wurde jeweils das sogenannte Spline Detrending Verfahren angewandt, bevor die Amplitude durch einen Sinusfit an die bereinigten Datenpunkte extrahiert wurde. Um die optimale Bereinigung des Langzeittrends zu erhalten, wurde die Spline-Methode weiter verbessert und eine Methode zur Bestimmung des besten Spline-Binnings entwickelt.

Während diesem Prozess wurden zwei Analysemethoden verglichen. Aufgrund der fixierten Endpunkte beim Spline Detrending Verfahren, wurden an beiden Seiten des Zeitintervalls entsprechend jeweils ein halbes Spline-Bin an Datenpunkten für die nachfolgende Analyse ausgelassen. Da dabei das Zeitintervall reduziert wird, wurde eine zweite Analysereihe eingeführt, die das volle Beobachtungsfenster in weiteren Auswertungen berücksichtigt. Bei der Auswertung zeigte sich aber, dass Letztere höhere χ^2_{red} Werte bei der Kurvenanpassung hat. Folglich wurde in der weiteren Analyse die erste Methode benutzt, bei der die Hälfte eines Spline-Bins an den Enden ausgeschlossen wird.

Mit der resultierenden Amplitude der Kurvenanpassung von der Sinusfunktion an die bereinigte Lichtkurve wurde dann die Dopplerthese getestet. Für die Interpretation der Variabilität wurde eine Gleichung hergeleitet, die auf dem Modell basiert, dass eines der beiden schwarzen Löcher im Zentrum einen Jet bildet, welcher dopplerverstärkt wird. Die Auswertung zeigte, dass die beobachtete Variabilität von PG 1553+113 und von PKS 2155-304 durch eine orbitale Dopplerverstärkung der Jet Emission des kleineren schwarzen Lochs erklärt werden kann. Darüber hinaus ist es bei PG 1553+113 sogar möglich, dass die Variabilität aus dem Jet des schwereren schwarzen Lochs stammt. Für die anderen drei Quellen PKS 0454-234, S5 0716+714 und OJ 014 ist die orbitale Dopplerhypothese nicht tragbar.

Für zukünftige Studien schlagen wir *Fermi*-Analysen von Photonen ab 1 GeV aufwärts vor, weil der Sinusverlauf dort stärker ausgeprägt ist. Außerdem raten wir zu einer Erweiterung der Dopplereffekt-Gleichung, um auch einen zweiten Jet, eine elliptische Umlaufbahn und die allgemeine Relativitätstheorie zu berücksichtigen. Abschließend wäre es interessant, die Hypothese auf die anderen Wellenbereiche anzuwenden und eine umfassende Studie mit den Beobachtungsdaten aus den verschiedenen Wellenlängen durchzuführen.

Contents

1	Introduction	1
2	Active Galactic Nuclei	2
2.1	Structure and Classification	2
2.2	Blazars and their intrinsic variability	5
2.3	Supermassive black hole binaries	5
2.4	Radiative Processes	7
2.4.1	Photon Scattering	8
2.4.2	Synchrotron radiation	10
3	Doppler-boost hypothesis	13
4	The <i>Fermi</i> Gamma-ray Space Telescope	17
4.1	The <i>Fermi</i> Large Area Telescope	17
4.2	Spectral Models	19
4.3	Maximum likelihood method	20
5	Analysis	22
5.1	Data acquisition	22
5.2	Amplitude Analysis	25
5.2.1	Overview on the analysis of the <i>Fermi</i> -LAT data	25
5.2.2	Detrending	28
5.2.3	Sine fitting	28
5.2.4	Determination of the best Spline binning	29
6	Evaluation of the Doppler-boost hypothesis	33
7	Discussion and Conclusions	41
8	Future perspectives	44
9	Summary	45

Chapter 1

Introduction

Since thousands of years humankind is interested in the astronomical phenomena depicted in the sky (e.g. see the Nebra sky disk [2]). With evolving technology and better instruments also the study of the astrophysics behind those stellar objects became an important topic during the past century.

The detection of gravitational waves, proposed by Einstein [3, 4], by the *Laser Interferometer Gravitational-Wave Observatory* (LIGO) in the United States and Virgo in Italy in the year 2015 (see Abbott et al. (2016) [5]) marked the beginning of a new field in multi-messenger astronomy. With the *Pulsar Timing Array* (PTA) the presence of a low-frequency gravitational wave background was shown [6, 7]. One possible source of such gravitational waves are *supermassive black hole binaries* (SMBHBs) that orbit in close vicinity. D’Orazio and Charisi (2023) [1] therefore aim to find reliable methods for discovering SMBHBs in *active galactic nuclei* (AGN).

A possible observable signature of SMBHBs could be the periodic variability caused by orbital Doppler boosting. In this thesis, the hypothesis of the flux changes originating from the Doppler effect will be tested on a core sample of five sources.

To get started, the theory, on which the Doppler-boost hypothesis is based on, is described in the following chapters. In the next chapter 2 the general model of AGN and Blazars, in particular, as well as the radiative processes and the evolution of SMBHBs are introduced. In the following one, an equation is derived to check the Doppler-boost hypothesis, and in chapter 4, the *Fermi* Large Area Telescope is introduced. The source selection and the acquiring of the data that is needed for the equation is described in detail in chapter 5 section 5.1. In the next section, the analysis method is explained. The results are shown in chapter 6 and are further discussed in the following one. In the end, a brief outlook will be given on future prospects of the Doppler-boost hypothesis.

Chapter 2

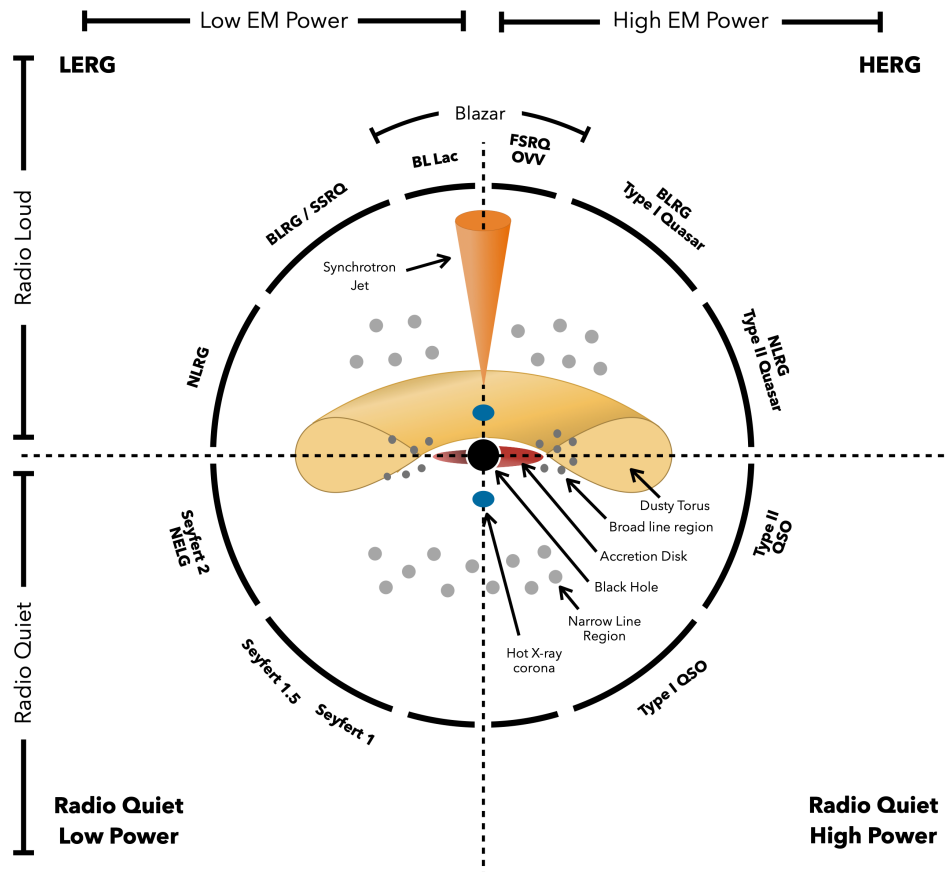
Active Galactic Nuclei

2.1 Structure and Classification

Among the billions of galaxies [8] a few stand out with their high bolometric luminosity in the range of $L_{bol} \sim 10^{41} - 10^{48}$ erg/s mainly coming from the centre of the galaxy [9]. Such cores are classified as AGN. The observed *electromagnetic* (EM) spectra of these are very distinctive and span across more than twenty orders of magnitude in frequencies [10]. AGN are very luminous compared to their size and shine brighter than the rest of the host galaxy. So it is assumed that other physical processes than the well-known nuclear fusion that powers stars take place in AGN [11]. With a *supermassive black hole* (SMBH) in the centre of the galaxy, the energy is mainly produced by mass accretion [10]. But also other non-thermal processes have to be considered when talking about AGN. Those will be explained in section 2.4.

Apart from the SMBH, the AGN consists of a corona, an accretion disk around the black hole, a dust torus possibly obscuring some line of sights, a *broad-line region* (BLR), a *narrow-line region* (NLR) and in rare cases collimated relativistic jets with outflowing material (see Figure 2.1).

Starting from the innermost layer the supermassive black hole with a mass of $\sim 10^5 - 10^{10} M_{\odot}$ [9], where M_{\odot} is the solar mass, is the main engine of the AGN. The heavier the SMBH is, the higher the luminosity of the AGN. That is because of the linear relation between the black hole mass and the Eddington Luminosity, which is the maximum luminosity of an object when there is an equilibrium between the gravitational force pulling matter inwards and the radiation pressure acting outwards. Furthermore, the luminosity is dependent on the steady supply of matter for the mass accretion happening in the SMBH. This is accomplished in the accretion disk where matter by losing angular momentum through viscous or turbulent processes gets pulled into the black hole. Instabilities in the accretion disk can strongly influence the accretion flow and thus, temporarily increase



J. E. Thorne

Figure 2.1: Schematic representation of the unified model of AGN. The supermassive black hole in the centre is surrounded by the accretion disk which supplies it with matter as well as the corona and the broad-line region. Encircling the centre is the dust torus which can obscure the BLR depending on the line of sight. Further out is the narrow-line region expanding far above and below the plane of the torus. The existing AGN subdivisions are assigned to the corresponding viewing angle, the existence of a jet and the EM power output. The figure was originally illustrated to be included in the introduction of Thorne et al. (2022) [12]. Reference for picture: Thorne et al. (2022) [13].

or decrease the luminosity. It is thought that those changes in the accretion flow are the main sources of the observed variability in AGN [10].

The close region around the SMBH is called the corona where charged particles move in a hot plasma with nearly relativistic speeds. Further out is the torus made out of gas and dust with a diameter of $1 - 10$ pc [10] which may obscure the line of sight at the inner parts (accretion disk, corona, BLR) depending on the orientation of the AGN. The BLR, which is located in between the dust torus, extends around the black hole and emits strong characteristic broad emission lines in the optical and the *ultraviolet* (UV) wavebands. Depending on the AGN orientation with respect to the line of sight of the observer, those broad lines can be affected by the torus. It is assumed that the BLR is made out of very fast-moving gas clouds with a high density in an orbit around the central SMBH [11]. The NLR lies outside the plane of the dust torus. Located far above and below it is always detectable regardless of the AGN orientation towards Earth. In the NLR the gas has a significantly lower density compared to the BLR and it is therefore possible to observe forbidden lines next to the narrow emission lines produced in this region.

Next to these main components of AGN, in some rare cases also relativistic jets form. Ranging from $10^{-7} - 10^6$ pc jets can far surpass the boundaries of their host galaxies. They are collimated beams of non-thermal plasma and the main source of gamma rays. Their EM emissions span across the radio up to the most extreme energetic gamma rays. With speeds near the speed of light, they undergo strong relativistic Doppler and aberration effects which affect the intrinsic luminosity of the jet and make it appear more bluish (reddish) and brighter (dimmer) when the jet faces towards (away from) us.

Depending on the orientation with respect to the observer's line of sight and the existence of jets, AGN are divided into different subclasses (see Figure 2.1). Starting with the existence of jets one distinguishes between jetted AGN with jets and non-jetted AGN without one. In the case of non-jetted AGN, it is distinguished between Seyfert 1 to Seyfert 2 and a Type I *quasi-stellar object* (QSO) and a Type II QSO. When jets are present, AGN are classified as radio-loud whereas with no jets they are called radio-quiet. Radio-loud AGN are divided depending on the orientation to Earth into *narrow-line region galaxies* (NLRG), *broad-line region galaxies* (BLRG), where, next to the narrow lines, also the broad emission lines from the BLR are visible, *steep spectrum radio quasars* (SSRQ) and blazars, where the jet points straight towards Earth and therefore dominates the spectrum of the AGN by being Doppler boosted. Blazars are subdivided into *BL Lacertae* (BL Lacs) and *flat spectrum radio quasars* (FSRQs). Furthermore, quasars of Type I and II are also radio-loud AGN with high EM power. For a more detailed classification see Padovani et al. (2017) [10].

As for this thesis, only the BL Lacs and the FSRQs are of particular interest as they show a distinct variability in their luminosity with time scales from seconds to many years.

2.2 Blazars and their intrinsic variability

According to Ackermann et al. (2015) [14], the gamma-ray sky is dominated by blazars. This type of AGN is characterised by its high and variable polarisation, high brightness temperatures, non-thermal continuum and superluminal velocities of compact radio cores [11]. Furthermore, one of its key features is its strong variability. Blazars display large flux changes from radio to very high energy and on multiple time scales of just a few minutes to over year-long time intervals. They are divided into BL Lacs and FSRQs depending on their optical spectra. BL Lacs show a featureless optical/ UV spectrum, whereas the FSRQs have an emission-line-dominated spectrum.

Blazars are jetted AGN, whose relativistic jet is close to the line of sight. Since the emission from the jet gets therefore Doppler boosted, the jet emission dominates the observed spectra from the AGN. Following that, the strong variability can be explained by changes in physical conditions or by geometrical interpretations. Based on the latter studies such as from Raiteri et al. (2017) [15] suggest that most of the fast flux variability at most frequencies is caused by the jet.

Most of the time we see random variabilities in the *light curves* (LCs) of blazars. However, in some cases, we observe hints for periodic patterns in the gamma-ray LCs (e.g. see Peñil et al. (2022) [16]). Due to the limited observation time, it is sometimes difficult to distinguish between both, because random processes happening in the blazar can mimic a periodic variability in the flux for a few cycles. Periodic ones, however, originate very likely from periodic processes inside the AGN and can provide therefore important information about the astrophysical nature of an AGN. But also external components could lead to time patterns in the LC (see for example gravitational lensing described in Postman (2012) [17] or in De Toma (2022) [18]).

Some of the currently possible theories behind periodic patterns are modulations in the accretion flow (e.g. Gracia et al. (2003) [19]), lighthouse effects in jets (e.g. Tavani (2018) [20] or Rieger (2004) [21]), or the existence of binary SMBHs (e.g. Celoria et al. (2018) [22]). Often it is also a combination of those (see for example Rieger (2007) [23] where the variability is explained through accretion disk interactions in the optical, through Newtonian jet precession in the radio and through orbital motion in the high energy bands).

2.3 Supermassive black hole binaries

As previously listed a possible explanation for the periodicity in the luminosity of AGN is a binary system of SMBHs in the centre of the AGN. Such SMBHBs are most likely the product of a merger event of two galaxies with each hosting a SMBH in the centre.

The probability of two SMBHs to pair at a given redshift is dependent on the SMBH occupation fraction and the galaxy merger rate at this redshift [1]. With those two factors, one gets the SMBH pairing rate and its distribution along the redshift. This rate can then tell us more about the evolution of our universe as the redshift correlates to the time at which the source is being observed. After the initial pairing of two SMBHs at \sim kpc scales, dynamical friction reduces the angular momentum in the system and the SMBHs evolve on the order of a galactic dynamical time ($\sim 10^8$ yr) into a, with respect to the surrounding stellar cluster, bound SMBHB at $\mathcal{O}(1 - 10)$ pc separation. During the large-scale evolution of the two SMBHs into a SMBHB, it is referred to as Dual AGN. For small-scale separations, the SMBHB evolution is mainly dominated by energy loss through gravitational radiation. Through the waves, both energy and angular momentum are extracted from the system. As a result, the semi-major axis decreases and the orbit gets circularised. This process becomes significant for the SMBHB evolution when the binary lifetime due to gravitational radiation gets shorter than the age of the universe [1].

The transition from the large-scale evolution to its gravitational radiation-dominated regime can be achieved through interactions with the immediate environment. Around ~ 1 pc the dynamical friction becomes less efficient, while the separation is still too large for a significant energy loss through gravitational radiation. Therefore, other processes must be taken into account to explain the energy reduction. Possible processes are SMBHB interactions with surrounding stars [24] or gas [25] that are torqued near the centre of the galaxy and hence lower the energy of the binary or interactions with a possible third black hole [26, 27]. Apart from interactions with objects inside the galaxy, also extragalactic sources like an incoming star cluster [28] or more generally a massive perturber [29] can lead to further energy losses [1].

The large-scale evolution in Dual AGN, where both SMBHs are accreting and therefore, outshine their host galaxy, can be observed in the optical, X-ray and radio bands. With the current observatories, it is possible to resolve Dual AGN systems down to ~ 8 kpc separation at redshift $z = 1$ in the X-ray waveband with Chandra and even down to 10 pc with the VLBI in the radio band [1].

Note that VLBI observations require the AGN to be bright in the radio frequencies, often characterized by the presence of a jet, which holds for less than 10% of the observed AGN population [30]. Furthermore, there exist other indirect detection methods where one looks for signatures that are linked to SMBHBs as a consequence of the binary system. For example, double-peaked emission lines occur when both SMBHs form their own narrow line region. That is because the emission lines are blue- or redshifted relative to the motion of the SMBHs given their opposite trajectories. For a more comprehensive and detailed review of the detection methods of Dual AGN see De Rosa et al. (2019) [31].

In the case of the small-scale evolution in SMBHB, only indirect methods can be applied since we are limited by the spatial resolution currently possible and cannot resolve sub-parsec structures in distant AGN (as for now). Current detection methods make use of spectral signatures, photometric signatures, jet signatures and direct measurements of gravitational waves. In D’Orazio and Charisi (2023) [1], the different signatures and their corresponding methods are discussed in detail. But as for this work, we will focus on the photometric signature of periodic variability.

These periodic patterns in the LC can be explained through multiple processes. One theory suggests variations in the accretion rate that arise through interactions of the SMBHB with its accretion disk resulting in accretion disk instabilities. Furthermore, binary self-lensing is expected to occur in binaries with sufficient inclination to the line of sight. Here the emission from one of the SMBHs gets lensed once per orbit by the other SMBH. The resulting lensing flare has approximately a duration of one-tenth of the period time of an orbit according to D’Orazio and Charisi (2023) [1]. Finally, we expect orbital Doppler boosting to occur due to relativistic, observation-angle-dependent effects when the emitting region is moving along the SMBHs. In this thesis, five promising SMBHB candidates will be analysed regarding the question of whether or not the periodic variability can be explained through orbital Doppler boost. A derivation of the Doppler effect can be found in the chapter 3.

2.4 Radiative Processes

To test the orbital Doppler-boost hypothesis using the periodic variability pattern, we first need to understand how and where the observed gamma rays are produced inside AGN. Radiative processes that should be considered for such highly energetic photons are synchrotron radiation and different variants of photon scattering. Through synchrotron radiation photons are emitted while through photon-particle interactions the energy of the photon can be both significantly decreased as well as increased leading to distinct spectral shapes of different emission zones within the AGN. The main source of gamma rays in an AGN is the jet with its relativistic plasma outflow of charged particles. As a result of the fast-moving charged particles inside magnetic fields, the jet emission is characterised by strong synchrotron radiation. The so-emitted photons get then up-scattered through inverse Compton scatterings into the gamma-ray-energies and above. This up-scattering can also apply to photons coming from the environment of the jet, e.g. the accretion disk, the corona, the BLR or the torus. So for the emission of gamma rays, both radiative processes have to be taken into account.

2.4.1 Photon Scattering

Beginning with the simplest case of photon-particle interaction the Thomson Scattering describes the nonrelativistic case where the photon has a significantly lower energy E than the rest energy of the particle,

$$E = h\nu \ll mc^2, \quad (2.1)$$

with the frequency ν of the electromagnetic wave and the mass m of the particle. Next to the general requirement of a free, charged particle, so that it can interact with the EM wave, the particle has to move at nonrelativistic speeds ($v \ll c$) for the Thomson scattering. Thus a classical approach of the interaction is possible, making it equivalent to a fully elastic scattering from classical physics. In this classical view, the particle of charge q absorbs the incoming photon and gets accelerated by the electric field of the photon. When the particle decelerates it emits a photon of the same energy as the incoming one. Depending on the orientation to the observer, the EM wave is after the scattering polarised or not [9]. The differential cross-section of this process can be defined as,

$$\frac{d\sigma}{d\Omega} = \frac{1}{2} (1 + \cos^2 \theta) r_e^2, \quad (2.2)$$

with the classical electron radius, $r_e = q^2/(mc^2)$. With the underlying symmetry in the angle θ , the radiation is equally scattered in the forward and backward directions. The total cross-section then results in,

$$\sigma_T = 2\pi \int_0^\pi \frac{d\sigma}{d\Omega} \sin \theta d\theta = \frac{8\pi}{3} r_e^2 = \frac{8\pi}{3} \left(\frac{q^2}{mc^2} \right)^2. \quad (2.3)$$

Because of the inverse quadratic dependence on the mass of the particle, the total cross-section for a photon scattering on a proton is of a factor of $(m_p/m_e)^2 \simeq 3.4 \times 10^6$ smaller than a scattering on an electron [9].

In plasma produced photons can all undergo Thomson scattering before leaving in the direction of the observer, thus making the Thomson scattering an important process to understand in many astrophysical sources.

A more general approach to photon-particle interaction is done in the Compton Scattering. Here the photon energy is not restricted. Thus it can have a comparable energy to the rest mass of the particle, which makes it necessary to consider quantum mechanic effects. The effective cross-section will be reduced in comparison to the Thomson case because of that. Also in quantum-mechanics, the photon has a momentum next to its energy and can transfer energy via the scattering to the charged particle. Like in all scattering processes, the amount of transferred energy is proportional to the change of direction of the photon,

with bouncing backwards being the largest energy transfer to the particle. The equation for that energy loss of the photon is,

$$\Delta E = h \Delta \nu = \frac{h c}{\Delta \lambda}, \quad (2.4)$$

with,

$$\Delta \lambda = \frac{h}{m c} (1 - \cos \theta). \quad (2.5)$$

This results in the energy E_2 of the photon after the Compton scattering,

$$E_2 = \frac{E_1}{1 + \frac{E_1}{m c^2} (1 - \cos \theta)}, \quad (2.6)$$

in relation to the photon energy E_1 before the scattering. With small initial photon energies, $E_1 \ll m c^2$, the Compton Scattering results in the Thomson scattering case and the energy of the incoming photon is the same as of the outgoing photon. Thus there is no energy transfer. The differential cross-section can be obtained by applying quantum electrodynamics. The resulting Klein-Nishina formula [9] is,

$$\frac{d\sigma}{d\Omega} = \frac{1}{2} r_e^2 f(\epsilon, \theta)^2 [f(\epsilon, \theta) + f(\epsilon, \theta)^{-1} - \sin^2 \theta], \quad (2.7)$$

with,

$$f(\epsilon, \theta) = \frac{1}{1 + \epsilon (1 + \cos \theta)}, \quad (2.8)$$

and the relation of the initial photon energy E_1 to the rest mass energy of the charged particle,

$$\epsilon = \frac{E_1}{m c^2} = \frac{h \nu_1}{m c^2}. \quad (2.9)$$

The total cross-section expressed with σ_T and ϵ is,

$$\sigma_{KN} = \frac{3\sigma_T}{4} \left\{ \frac{1 + \epsilon}{\epsilon^3} \left[\frac{2\epsilon(1 + \epsilon)}{1 + 2\epsilon} - \ln(1 + 2\epsilon) \right] + \frac{\ln(1 + 2\epsilon)}{2\epsilon} - \frac{1 + 3\epsilon}{(1 + 2\epsilon)^2} \right\}. \quad (2.10)$$

According to approximations of this expression, Compton scattering becomes very inefficient for high photon energies. This is known as the Klein-Nishina effect, according to which photons can achieve energies in the MeV to TeV region. As a result, the Klein-Nishina effect has important consequences for the interpretation of the spectral energy distribution of AGN.

Opposed to Compton scattering, where the photon transfers energy to the charged particle, in cases of particles moving at relativistic speeds, the energy can be transferred to the

low-frequency photon in the Compton process. This is called the inverse Compton scattering. In this relativistic treatment of the scattering problem, the condition for Thomson scattering $h\nu \ll mc^2/\gamma$ is again fulfilled in the rest frame and thus the cross-section corresponds to that of Klein-Nishina. With the Lorentz factor defined as,

$$\gamma \equiv \frac{1}{\sqrt{1 - \frac{v^2}{c^2}}}, \quad (2.11)$$

the energy E_2 after the inverse Compton scattering of the photon with initial energy E_1 is,

$$E_2 \simeq \gamma^2 E_1. \quad (2.12)$$

The resulting luminosity L_{IC} contributed by the inverse Compton effect is proportional to,

$$L_{IC} \propto n_{ph} \gamma^2 E_1, \quad (2.13)$$

where next to the quadratic dependence on the Lorentz factor also the dependence on the photon density n_{ph} is described. Hence, in regions with large amounts of photons and relativistic electrons, their interaction results in high-energy radiation. Therefore, the inverse Compton scattering process is an important source of X- and gamma rays in an AGN.

For a more detailed explanation and the exact derivation of the physics behind the inverse Compton effect and the other scattering processes as well as the following synchrotron processes see "Radiative Processes in Astrophysics" by Rybicki and Lightman (1991) [32].

2.4.2 Synchrotron radiation

When a charged particle moves through an electromagnetic field the Lorentz force applies and bends the trajectory perpendicular to the direction of the magnetic field. Because of this acceleration, the particle emits synchrotron radiation. With higher relativistic speeds of the particle, the emission gets more beamed toward the direction of motion. The opening angle of the synchrotron emission cone is proportional to the inverse of the Lorentz factor of the charged particle. One prominent example of the origin of synchrotron radiation in AGN is the jet. Here particles move at relativistic speeds along the plasma outflow away from the SMBH. Through the magnetic fields inside the jet, a circular motion gets induced and the charged particles follow a helical path (Figure 2.2).

The component corresponding to the synchrotron luminosity can be written as,

$$L_S = \frac{4 Z^4 e^4 B^2 \gamma^2 v^2}{9 c^5 m^2} = -\frac{dE}{dt} = \frac{4 Z^4 e^4 B^2 E^2}{9 m^4 c^7}, \quad (2.14)$$

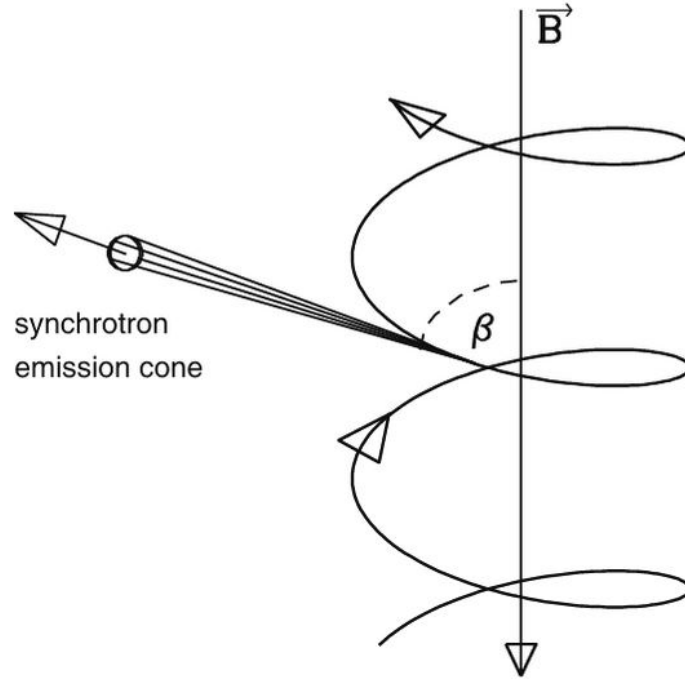


Figure 2.2: Schematic overview of the synchrotron radiation of a rotating electron. The charged particle moves along the helical path upwards while the magnetic field \vec{B} points downwards. β describes the pitch angle between the direction of motion and the magnetic field. Through the constant change of motion, the electron emits synchrotron radiation in the form of a cone with an opening angle $\phi \simeq \gamma^{-1}$. The picture was adapted from Beckmann and Shrader (2012) [9].

with the particle charge $q = Ze$, velocity v , mass m and energy E of the particle and the surrounding magnetic field B (see [9] for further derivation).

According to the $L \propto m^{-2}$ proportionality, the process is most efficient for electrons and positrons in comparison to heavier particles like protons. In the case of a proton jet, it would need to be significantly faster and/or more massive than an electron or positron jet to have a comparable synchrotron luminosity.

But as a consequence in a proton jet photons of higher energy would be possible as the expected proton-synchrotron peak would be at 10 – 100 GeV due to the increased mass of the radiating particle [33].

In the next step, we sum up over all single particle contributions from the plasma emitting synchrotron radiation, because not only is a single particle but a large number of charged particles responsible for the observed emission.

In the case of electrons with energies in the range from E_1 to E_2 , the total synchrotron emissivity expressed as the power per unit frequency and unit volume is,

$$\epsilon(\nu) = \int_{E_1}^{E_2} L(E, \nu) n(E) dE, \quad (2.15)$$

where $L(E, \nu)$ is the power per unit frequency and $n(E) dE$ is the number density of electrons in the energy interval between E and $E + dE$. As the energy distribution of astrophysical sources typically follows a power law one can write the particle density as a function of the electron energy,

$$n(E) dE = k E^{-p} dE, \quad (2.16)$$

with the normalisation k of the power law and the power law index p . This leads to the proportionality between emissivity and frequency,

$$\epsilon(\nu) \propto \nu^{-\alpha}, \quad (2.17)$$

with spectral index α described as,

$$\alpha = \frac{p-1}{2}. \quad (2.18)$$

As a result of the maximum critical frequency $\nu_{c,max}$, for electrons, there is a high energy cutoff detectable in the synchrotron spectrum of the AGN.

Earlier in this section, it was described how a photon can be up-scattered by a relativistic charged particle. Depending on the Lorentz factor γ of the particle, the inverse Compton scattering can increase the energy of radio and infrared photons into the X-ray or gamma-ray energy regimes. A special case is when the photons provided by the synchrotron emission then inverse Compton scatter with the same electron population responsible for their production. This combination of synchrotron radiation and inverse Compton scattering is called *synchrotron self-Compton* (SSC). For that to happen the plasma needs to be optically thick. But if all conditions are met, multiple SSCs can occur, leading to very energetic photons.

Doppler-boost hypothesis

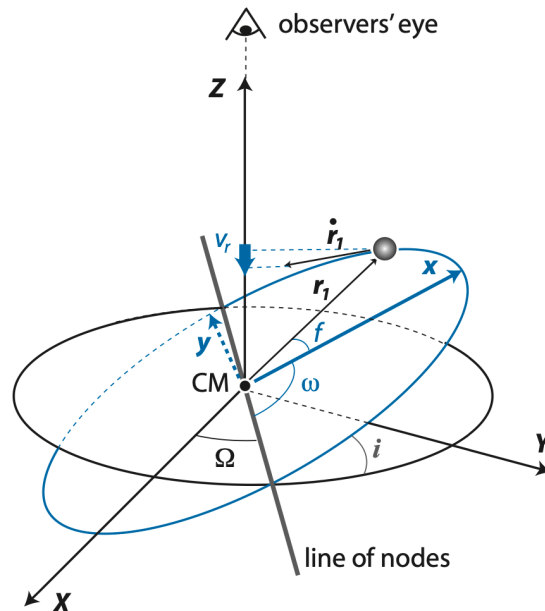


Figure 3.1: Depiction of the model for Doppler boosting. The smaller SMBH is orbiting the heavier one in the *centre of mass* (CM). The observer’s line of sight aligns with the Z-axis while the X- and Y-axes define the plane of the sky. The orbit is inclined at an angle i with respect to the plane of the sky. Image Credit: Charisi et al. (2022) [34].

The basic model of the Doppler-boost hypothesis is that we have two SMBHs orbiting each other in the centre of the AGN. It is assumed that both have a mini-accretion disk. Since usually they differ in mass the heavier one is closer to the *centre of mass* (CM) and the smaller SMBH is located on a less stable orbit around the CM compared to the more massive one. The binary mass ratio is defined as, $q \equiv \frac{M_2}{M_1}$, with $M_2 \leq M_1$ where M_1 and M_2 are the masses of the SMBHs respectively. If we observe Doppler boosting from both components the opposite movement directions will result in a decrease of the

total Doppler effect which corresponds to a dimming in luminosity compared to a single boosted object. But because the orbit of the smaller SMBH is less stable and it moves at higher velocities, it typically dominates the variability and we therefore account only for the Doppler effect of the smaller SMBH.

For the derivation of the Doppler boost we make the basic assumption that the emission of the source follows a power law, $F_\nu \propto \nu^{-\alpha_\nu}$, (as defined in section 2.4.2) in the observed wave band. The ratio of observed and emitted frequencies corresponds to the Doppler factor D ,

$$D \equiv \frac{\nu}{\nu'} = \frac{1}{\gamma(1 - \vec{\beta} \cdot \hat{n})} = \frac{\sqrt{1 - \beta^2}}{1 - \vec{\beta} \cdot \hat{n}}, \quad (3.1)$$

which is dependent on the Lorentz factor, $\gamma \equiv (1 - \beta^2)^{-1/2}$, and the line of sight velocity $\vec{\beta} \cdot \hat{n}$ with $\vec{\beta} \equiv \frac{\vec{v}}{c}$, the source velocity vector \vec{v} over the speed of light c , and the normalised line of sight vector \hat{n} . Important to note is that all emitting regions of the AGN have their own Doppler factor based on their configuration.

For all derivations of the Doppler boost the SMBHB geometrical model depicted in Figure 3.1 is used where the smaller SMBH orbits around the CM at an inclination I with respect to the plane of the sky.

The general relation between the flux F in the observer frame and F' in the frame of the emitting SMBH for the Doppler effect in AGN with a SMBHB is,

$$F_\nu = D_{orb} D_{rad}^{2+\alpha_\nu} F'_\nu, \quad (3.2)$$

where D_{orb} is the Doppler factor of the orbital motion of the smaller SMBH and D_{rad} is the Doppler factor correlating to the emitting part of the AGN responsible for the observed photons. The exponent of $2 + \alpha_\nu$ with the spectral index α_ν is due to the effect of aberration in extragalactic sources.

In the derivation of D'Orazio and Charisi (2023) [1] it was assumed that the photons originate from the accretion disk. This is true for optical and ultraviolet light, but not for gamma rays.

Disk based approach

When the photons are emitted in the accretion disk, the Doppler factor of the orbiting motion and the radiating source are equal. Thus, equation 3.2 simplifies to,

$$F_\nu = D^{3+\alpha_\nu} F'_\nu, \quad (3.3)$$

with the orbital velocity β_{orb} and the Lorentz factor γ of the smaller SMBH.

The resulting first-order expansion in the orbital velocity β_{orb} is,

$$F_\nu = \left[1 + (3 + \alpha_\nu) \beta_{orb} \cos \left(\frac{2\pi}{P} t \right) \sin I \right] F'_\nu. \quad (3.4)$$

A sinusoid with the same period P as the orbital motion of the SMBHB and amplitude A as a function of the spectral index α_ν , the orbital velocity β_{orb} and the inclination I ,

$$A_\nu = (3 + \alpha_\nu) \beta_{orb} \sin I. \quad (3.5)$$

β_{orb} can be written as a function of the binary mass ratio q ,

$$\beta_{orb} = [(1 + q)^2 2N_a]^{-1/2}, \quad (3.6)$$

with the number of Schwarzschild radii,

$$N_a := \frac{a}{\left(\frac{2GM}{c^2} \right)}, \quad (3.7)$$

where a corresponds to the semi-major axis of the orbit, G to the gravitational constant and M to the total mass of the SMBHB (derivation adapted from [1]).

As previously done in Tavani et al. (2018) [20] one obtains via Kepler's law the relation,

$$a^3 = \frac{P'^2}{4\pi^2} G M. \quad (3.8)$$

In the frame of the SMBHB the period time P' is equal to,

$$P' = \frac{P_{obs}}{(1 + z)}, \quad (3.9)$$

where P_{obs} is the observed period and z is the redshift. Combining those equations results in,

$$\beta_{orb} = \frac{1}{(1 + q) c} \left(\frac{2\pi G M (1 + z)}{P_{obs}} \right)^{1/3}, \quad (3.10)$$

for the smaller SMBH and according to Charisi et al. (2022) [34] in,

$$\beta_{orb, massive} = \frac{q}{(1 + q) c} \left(\frac{2\pi G M (1 + z)}{P_{obs}} \right)^{1/3}, \quad (3.11)$$

for the more massive SMBH.

Jet based approach

For the analysis of the Doppler effect in the gamma-ray waveband, one has to change the radiating source from the mini-disk to the jet of the SMBH as gamma rays are mainly observed from jets and are not directly associated with the emission from the accretion disks. Hence, D_{orb} and D_{rad} from equation 3.2 are now different. The Doppler term coming from the aberration equals,

$$D_{jet}^{2+\alpha_\nu} = \left(\frac{\sqrt{1 - \beta_{jet}^2}}{1 - \vec{\beta}_{jet} \cdot \hat{n}} \right)^{2+\alpha_\nu}, \quad (3.12)$$

in the jet frame, hence, called D_{jet} instead of D_{rad} , with the parameters, $\vec{\beta}_{jet} = \frac{\vec{v}_{jet}}{c}$, dependent on the velocity of a blob in the jet and the direction the jet is pointing towards us θ . Thus, $\vec{\beta}_{jet} \cdot \hat{n} \equiv \beta_{jet} \cos \theta$, being maximal when the jet points directly towards Earth at an angle of $\theta = 0^\circ$. The other Doppler term coming from the orbital motion of the smaller SMBH and, therefore, the source of the jet can be written as,

$$D_{orb} = \left(\frac{\sqrt{1 - \beta_{orb}^2}}{1 - \vec{\beta}_{orb} \cdot \hat{n}} \right). \quad (3.13)$$

For D_{orb} , the formula derived in the disk case from above can be applied.

The assumptions for the jet approach are that the jet is fixed in relation to its source (the SMBH) and its direction towards Earth, and that it does not deform while the small SMBH moves around. Also, the possible precession of the jet is neglected for the sake of simplicity. For that one could add another sinusoidal wave on top of the current one. As a result the velocity at line of sight $\beta_{jet} \cdot \hat{n}$ would change to $\beta_{jet} \cos \theta \cdot prec(t)$.

The resulting first-order expansion for the jet-based approach in the orbital velocity is,

$$F_\nu = \left[1 + \beta_{orb} \cos \left(\frac{2\pi}{P} t \right) \sin I \right] D_{jet}^{2+\alpha_\nu} F'_\nu, \quad (3.14)$$

which leads to a flux amplitude of,

$$A_\nu = \beta_{orb} \sin I \cdot D_{jet}^{2+\alpha_\nu}. \quad (3.15)$$

This can be further expanded to the first order in the jet velocity β_{jet} ,

$$A_\nu = \beta_{orb} \sin I [1 + (2 + \alpha_\nu) \beta_{jet} \cos \theta], \quad (3.16)$$

thus leading to an equation with four unknown parameters (binary mass ratio q , Inclination I , jet velocity β_{jet} and jet direction θ). Including equation 3.10 this can be written as,

$$A_\nu = \frac{1}{(1+q)c} \left(\frac{2\pi G M (1+z)}{P_{obs}} \right)^{\frac{1}{3}} \sin I [1 + (2 + \alpha_\nu) \beta_{jet} \cos \theta], \quad (3.17)$$

the final equation for the amplitude that will be used to test the Doppler-boost hypothesis.

Chapter 4

The *Fermi* Gamma-ray Space Telescope

Formerly known as the *Gamma-ray Large Area Space Telescope* (GLAST), the *Fermi* Gamma-ray Space Telescope was launched on 11th June, 2008 [35]. After its successful launch NASA renamed it in honour of the Italian-American scientist Enrico Fermi who was the first to propose one of the cosmic ray acceleration mechanisms, in 1949, leading to many of the high energy gamma rays detected by the telescope [36]. The satellite accommodates two instruments. The *gamma-ray burst monitor* (GBM) is designed to detect transient phenomena in the energy range of 8 keV to 40 MeV such as gamma-ray bursts. The *large area telescope* (LAT) observes the entire sky every three hours and is the main instrument. It can detect gamma rays with energies from below 20 MeV up to more than 300 GeV. The LAT has been in operation since 4th August, 2008.

The satellite is located on an orbit at an altitude of ~ 565 km and an inclination of 25.6° with respect to the equator. Earth's magnetosphere protects the telescope partially from cosmic radiation.

4.1 The *Fermi* Large Area Telescope

The *Fermi*-LAT is a pair-conversion telescope (Figure 4.1). It is based upon the physics of pair production, where a highly energetic photon interacts with nearby matter or other photons and forms a particle and its antiparticle. As a high-Z converter material, it uses tungsten to optimise the interaction probability of the incoming photon to do pair production. The produced electron-positron pair is then tracked via silicon strip detectors to measure the photon direction and energy. As a result of the high energy of the incoming photon, the electron-positron pair that is being produced follows predominantly the direction of the initial photon. Subsequently, the reconstructed direction of the incoming photon is limited by the scatterings of the pair components in the tracker and by the spatial resolution of the tracker. To measure the total energy of the incoming photon, a

calorimeter made of CsI(Tl) is positioned at the bottom of the tracker module. With its 96 CsI crystals doped with thallium it can obtain both longitudinal and transverse information about the energy distribution pattern of the particle shower. The LAT is structured as a 4×4 array of different modules. Each one consists of a tracker, a calorimeter and a tower electronic module responsible for control and data acquisition. The tracker array is surrounded by 89 tiles of plastic scintillators forming the *anti-coincidence detector* (ACD). Its function is to reject the charged particle background.

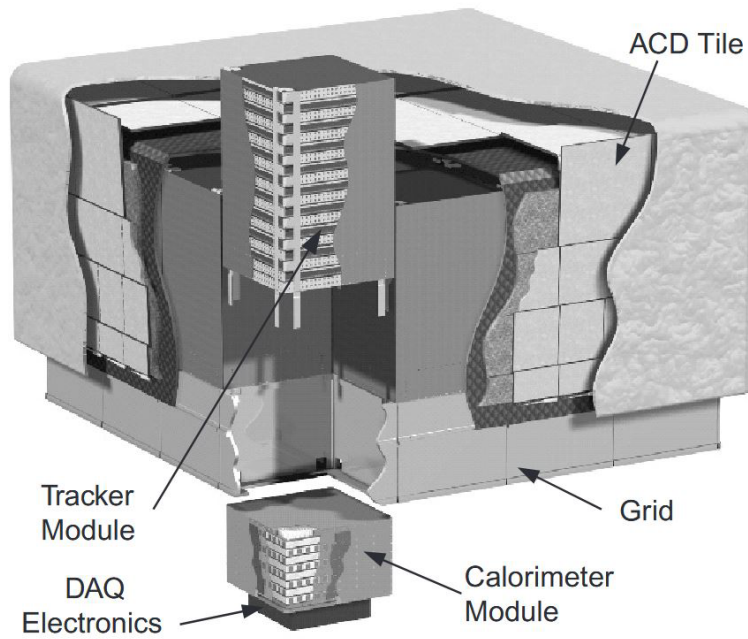


Figure 4.1: Cut-away Depiction of the LAT instrument adapted from Johnson and Mukherjee (2009) [37]. The tracker modules are surrounded by the ACD. Underneath each tracker module is a calorimeter followed by the *tower electronics module* (TEM). The TEM is made of a programmable trigger and the *data acquisition system* (DAQ).

Since *Fermi* has only a downlink rate of ~ 400 Hz the collected data first has to be analysed and filtered onboard before it can be transmitted to Earth. The *data acquisition system* (DAQ) therefore takes the information from the other modules and reduces the trigger rate from 2 – 3 kHz. The concrete procedure can be found in Atwood et al. (2009) [35]. For the evaluation of LATs performance, the *instrument response functions* (IRFs) were derived from Monte Carlo simulations. The IRFs are high-level models depending on several parameters such as the photon energy, incidence angle and conversion point within the instrument.

4.2 Spectral Models

To evaluate equation 3.17, α_ν , which is equal to the spectral index α , is required. D’Orazio and Charisi (2023) [1] assumed therefore in their model a Power Law spectrum for the source, as it is a basic and relatively good approximation of AGN. It describes the general behaviour of a wide range of physical processes like synchrotron radiation or inverse Compton scattering while still being very simple. The implementation in *Fermi* is,

$$\frac{dN}{dE} = N_0 \left(\frac{E}{E_0} \right)^{-\alpha}, \quad (4.1)$$

with only the three parameters: the prefactor N_0 , the spectral index α , which is expected to be 2.0, and the energy scale E_0 .

For some sources, the spectral shape differs significantly from a simple power law, for which more sophisticated models have to be applied. Another model found to obtain good results in such cases is the Log Parabola model, which introduces an additional parameter β accounting for the curvature in the spectrum. The formula for Log Parabola is then given by,

$$\frac{dN}{dE} = N_0 \left(\frac{E}{E_b} \right)^{-(\alpha + \beta \ln(E/E_b))}, \quad (4.2)$$

with the norm N_0 , spectral index α and pivot energy E_b [38]. As in the Power Law, the Log Parabola has also a parameter α accounting for the spectral index. This value will be used for the sources that have a Log Parabola spectrum.

Another model that will be relevant later for the sample of sources analysed in this work is described as a power law with a super-exponential cutoff (denoted by `PLSuperExpCutoff4` in the *fermipy* documentation¹), usually only used for pulsar-like sources. This model introduces even more parameters to successfully fit the spectrum and is defined as follows,

$$\frac{dN}{dE} = \begin{cases} N_0 \left(\frac{E}{E_0} \right)^{-\alpha_0 - \frac{d}{2} \ln(\frac{E}{E_0}) - \frac{d \cdot b}{6} \ln^2(\frac{E}{E_0}) - \frac{d \cdot b^2}{24} \ln^3(\frac{E}{E_0})}, & \text{if } |b \ln(\frac{E}{E_0})| < 1e^{-2} \\ N_0 \left(\frac{E}{E_0} \right)^{-\alpha_0 + d/b} \exp\left(\frac{d}{b^2} (1 - (\frac{E}{E_0})^b)\right) & \text{otherwise} \end{cases}, \quad (4.3)$$

with the prefactor N_0 , the index α_0 corresponding to the spectral index from previous models, the energy scale E_0 , the exponential factor d and a second Index b [38].

At E_0 the prefactor N_0 corresponds to the normalisation of the flux density, α_0 is the local spectral index and d is the local curvature.

When $b = 0$ this spectral model devolves into a Log Parabola with $\alpha = \alpha_0$ and $\beta = d/2$. As for that, the index α_0 is used as spectral index in all following computations.

¹https://fermi.gsfc.nasa.gov/ssc/data/analysis/scitools/source_models.html#LogParabola

4.3 Maximum likelihood method

For the evaluation of the observed photon events, the maximum likelihood method is applied. It is used to compare the measured counts versus the expected counts and to estimate the best set of parameters α_k for a given model, also referenced as hypothesis H_1 .

For the analysis, the photon counts are binned into many different bins in energy and spatial intervals. Thus, the large amount of initial counts is divided into bins with only a small number of counts. For each bin, the Poisson distribution describes the observed number of counts. The expected number of counts in the i -th bin is here denoted as $\phi_i(\vec{\alpha})$ and is dependent on the source model with its several parameters α_k . The probability of observing n counts in a bin is according to Poisson,

$$p(n, \phi) = \frac{\phi^n}{n!} e^{-\phi}, \quad (4.4)$$

with the expected value ϕ in this bin.

To get the overall likelihood \mathcal{L} for each hypothesis, one multiplies over all bin probabilities of observing n_i counts with given model $\vec{\alpha}$,

$$\mathcal{L}(\vec{\alpha}) = \prod_i p(n_i, \phi_i(\vec{\alpha})) = \prod_i \frac{\phi_i(\vec{\alpha})^{n_i}}{n_i!} e^{-\phi_i(\vec{\alpha})} = e^{-\phi_{tot}(\vec{\alpha})} \prod_i \frac{\phi_i(\vec{\alpha})^{n_i}}{n_i!}, \quad (4.5)$$

with the total number $\phi_{tot}(\vec{\alpha})$ of expected counts. The higher the given likelihood value, the better is the agreement between model and data. Therefore, the best fit with its set of parameters $\vec{\alpha}_k$ can be found by maximising the likelihood. In order to do this, it is more efficient to use the logarithm,

$$\log \mathcal{L}(\vec{\alpha}) = \sum_i n_i \log \phi_i(\vec{\alpha}) - \sum_i \phi_i(\vec{\alpha}) - \sum_i \log(n_i!). \quad (4.6)$$

This splits the product into three sums. Since the last term is independent of the source model it can be neglected in the optimisation. Furthermore, the sum over all expected counts ϕ_i can be written as the total number of predicted counts ϕ_{tot} . Thus leading to,

$$\log \mathcal{L}(\vec{\alpha}) = \sum_i n_i \log \phi_i(\vec{\alpha}) - \phi_{tot}(\vec{\alpha}). \quad (4.7)$$

The statistical errors for the best-fit parameters can be found via the maximum error. With an upper limit to the covariance matrix derived in H. Cramer (1946) [39] and in R. C. Rao et al. (1945) [40] the error can be estimated with,

$$\sigma_{ab}^2 = \left[- \frac{\partial^2 \log \mathcal{L}}{\partial \alpha_a \partial \alpha_b} \bigg|_{\{\vec{\alpha}_k\}} \right]^{-1}. \quad (4.8)$$

To determine the quality of the model, the residuals are computed. The significance of the residual at map position (i, j) can be written as,

$$\sigma_{ij}^2 = 2 \operatorname{sgn}(\tilde{n}_{ij} - \tilde{m}_{ij}) (\ln \mathcal{L}_P(\tilde{n}_{ij}, \tilde{n}_{ij}) - \ln \mathcal{L}_P(\tilde{n}_{ij}, \tilde{m}_{ij})) , \quad (4.9)$$

with,

$$\tilde{m}_{ij} = \sum_k (m_k \cdot f_k)_{ij} \quad \wedge \quad \tilde{n}_{ij} = \sum_k (n_k \cdot f_k)_{ij} \quad \wedge \quad \ln \mathcal{L}_P(n, m) = n \ln(m) - m . \quad (4.10)$$

The data and model maps at energy plane k are denoted as n_k and m_k . The convolution kernel, which is proportional to the expected counts at a given pixel, is called f_k and is normalised as,

$$f_{ijk} = s_{ijk} \left(\sum_{ijk} s_{ijk}^2 \right)^{-1} , \quad (4.11)$$

with s being the expected counts cube of a pure signal normalised to one [41].

The significance of the data/ model residual can be then plotted against their coordinates. This enables a graphical evaluation of the goodness-of-fit of the model. The goal is a residual map with no deviations of the model and the smoothed data, which would correlate to an excess or a deficiency of photon counts, within the *region of interest* (ROI).

While the residual takes both positive and negative deviations into account, the *test statistic* (TS), however, does only consider positive ones. In the case of the TS, one tests the hypothesis H_1 (i.e. the presence of a source at a specified position in the sky) with the model where the source is included against the null hypothesis H_0 with the source excluded from the model. According to Wilks' theorem, the TS can be written as,

$$TS = -2 \log \left(\frac{\mathcal{L}_{max, H_0}}{\mathcal{L}_{max, H_1}} \right) , \quad (4.12)$$

where \mathcal{L}_{max, H_0} and \mathcal{L}_{max, H_1} are the maximised likelihoods for the hypothesis H_0 and H_1 . Since TS is monotonically increasing with \mathcal{L}_{max, H_1} , maximising the likelihood is equivalent to maximising the TS. Following Wilks' theorem the TS is in the limit of a large number of counts asymptotically distributed as the χ_x^2 -distribution with x degrees of freedom. x is the number of parameters characterising the additional source in H_1 . The higher the TS value is, the more unlikely becomes the null hypothesis. Following the basic rule of thumb, the square root of the TS is approximately equal to the detection significance for a given source [42].

Chapter 5

Analysis

5.1 Data acquisition

In the following, we now want to test whether the Doppler-boost hypothesis given by equation 3.17 is fulfilled for a selected sample of promising sources. These sources have already been studied before and show hints to host a binary system of black holes. Since our previously derived equation is highly degenerate, given the amount of free parameters, we first performed a literature search to minimise the number of unknown variables.

The values used for this analysis are listed in the following section. Apart from the parameters that can be looked up in previous studies, the amplitude is obtained through a sine fit onto the detrended gamma-ray LC. In section 5.2 this is explained in more detail.

Sample: For the evaluation of the Doppler-boost hypothesis, a test sample of five sources was established. The sources are stated in Table 5.1. Among the thousands of AGN, those were selected because they show a significant variability pattern that very likely does not arise from the intrinsic variability of blazars. The periodicity and its significance are studied in Peñil et al. (2022) [16]. The five sources with high periodicity probability were taken for this thesis as the core sample.

Total binary mass: In Table 5.2, the total SMBHB masses of the five sources are listed. The error for the values from Xiao et al. (2022) [43] were given for $\log_{10}(M_{BH})$. With $\sigma_{\log M}$, the error can be obtained following,

$$\sigma_M = \sigma_{\log M} \cdot M_{BH} \cdot \ln 10, \quad (5.1)$$

4FGL source name	Association name	RA (J2000) [°]	Dec (J2000) [°]	Type
J0457-2324	PKS 0454-234	74.26096	-23.41384	FSRQ
J0721.9+7120	S5 0716+714	110.48882	71.34127	BL Lac
J0811.4+0146	OJ 014	122.86418	1.77344	BL Lac
J1555.7+1111	PG 1553+113	238.93169	11.18768	BL Lac
J2158-3013	PKS 2155-304	329.71409	-30.22556	BL Lac

Table 5.1: Test sample for the evaluation of the Doppler-boost hypothesis. The five sources were selected, because they depict a high probability of periodicity in their LC (see Peñil et al. (2022) [16]).

which is derived from Gaussian error propagation [44] of,

$$M_{BH} = 10^{\log M}, \quad (5.2)$$

$$\sigma_M = \sqrt{\left(\frac{\partial M}{\partial(\log M)}\right)^2} \sigma_{\log M} = \ln 10 \cdot M \cdot \sigma_{\log M}. \quad (5.3)$$

In the cases with no provided error, the error is assumed to be 0.4 dex [45]. The error corresponds to,

$$\sigma_M = 0.4 \cdot M_{BH} \cdot \ln 10. \quad (5.4)$$

sources	SMBHB mass [M_\odot]	Notes
PKS 0454-234	$(2.14 \pm 0.69) \times 10^8$ [0.14] ¹	Estimated in Xiao+ (2022)[43]
S5 0716+714	$(1.20 \pm 1.11) \times 10^8$	Estimated from the variability timescale in Zheng+ (2008)[46]
OJ 014	$(5.13 \pm 8.15) \times 10^8$ [0.69] ¹	Estimated in Xiao+ (2022)[43]
PG 1553+113	$(4.3 \pm 4.0) \times 10^9$	Estimated from modelling in Chen+ (2024)[47]
PKS 2155-304	$(8.13 \pm 7.48) \times 10^8$	Estimated from modelling in Chen+ (2023)[48]

Table 5.2: Total SMBHB masses (in units of solar masses M_\odot) were provided in courtesy of Alessandra Azzollini.

Spectral index: As for the spectral index the values listed in Table 5.3 are taken from the catalogue 4FGL-DR4 [49], the fourth data release of the 4FGL catalogue of *Fermi*. Apart from S5 0716+714, which has a power law with a super-exponential cutoff spectral model, all other sources are best described by a Log Parabola. The individual parameters are retrieved from the catalogue as explained in section 4.2.

¹ Error was given for the decadic logarithm of the total mass. When no error was given the standard error of 0.4 dex was assumed [45].

sources	spectral index α	spectral model
PKS 0454-234	2.1021 ± 0.0091	Log Parabola
S5 0716+714	2.0288 ± 0.0078	PLSuperExpCutoff4
OJ 014	2.006 ± 0.029	Log Parabola
PG 1553+113	1.566 ± 0.017	Log Parabola
PKS 2155-304	1.8039 ± 0.0086	Log Parabola

Table 5.3: Spectral indices are taken from the 4FGL-DR4 catalogue [49]. In section 4.2 it is described, which parameter in each spectral model is associated with the spectral index α .

Period: For the evaluation of the period time, there exist several different methods each with their respective advantages and disadvantages. In Peñil et al. (2022) [16] the most prominent methods are being compared. According to Peñil (priv. comm.) the best method is the *generalised Lomb-Scargle periodogram* (GLSP, [50]) because it is the only one that takes also the errors of the data points into account. Hence, the period results from the GLSP performed in the paper of Peñil et al. [16] will be used. For reference, the averaged period over all methods as well as the period time obtained through GLSP are listed in Table 5.4. Note that the GLSP period does not differ much from the average period time. Therefore, the GLSP is a good representative.

For S5 0716+714 two significant periods were obtained through different methods. Since GLSP found only the (2.6 ± 0.4) yr period it will be used for the sine fit. Furthermore, it should be mentioned that the statistical confidence of the secondary period of 0.9 yr is significantly lower (see Peñil et al. (2022) [16]).

sources	Averaged Period (yr)	GLSP (yr)	redshift
PKS 0454-234	3.6	3.5 ± 0.4	1.003 [51]
S5 0716+714	2.7*	2.6 ± 0.4	0.241 ± 0.014 [52]*
OJ 014	4.1	4.1 ± 0.4	1.148 [53]
PG 1553+113	2.2	2.1 ± 0.2	0.360 [54]
PKS 2155-304	1.7	1.7 ± 0.1	0.116 ± 0.002 [55]

Table 5.4: In this table the period times obtained in Peñil et al. (2022) [16] as well as the redshifts are listed. It is distinguished between the averaged period time over all methods and the value obtained through GLSP, which will be used in further analysis. For the redshifts, most of them were measured using emission lines. *For S5 0716+714 a second 0.9 yr period was observed with methods other than the GLSP. Furthermore, the redshift of S5 0716+714 could not be measured due to the absence of emission lines and thus it was estimated as an upper limit for the redshift using the Ly α forest.

Redshift: In Table 5.4 also the redshift of each source is stated. For the majority, the redshift was measured using the observed spectrum. Only for S5 0716+714, it was estimated as an upper limit from the Ly α forest in the UV spectra due to the absence of optical lines [52].

5.2 Amplitude Analysis

5.2.1 Overview on the analysis of the *Fermi*-LAT data

Extraction of data

For the analysis, the data of the ROI was downloaded from the FSSC website². This provides several FITS files, the standard data format in astronomy for arrays and tables. The FITS files are organised in *header-data units* (HDUs), where the HDU itself is an array or table. For each object, we consider an ROI with a radius of 16° around its position (in the J2000 coordinate system). We then take the total photon events in the energy range from 100 MeV to 300 GeV during the time interval from the beginning of *Fermi*-LAT at 2008-08-04 15:43:36 UTC until 2024-03-07 12:04:23 UTC or in the case of OJ 014 until 2024-03-07 10:25:32 UTC. The exact search parameters for each source are stated in the Tables 1 - 5 in the appendix.

The above-described extraction method gives us several files labelled with "PH", the *Fermi*-LAT event files, and the definition of *good time intervals* (GTI) included in the spacecraft file with the label "SC". Only in the GTI can the data be considered valid for scientific purposes, while *Fermi* crosses the *southern Atlantic anomaly* (SAA), for example, the data is neglected.

Analysis of *Fermi*-LAT data

To obtain the gamma-ray LC, the *fermipy*³ package was used for the analysis of the *Fermi*-LAT data. At the beginning of the *Fermi* analysis, the events are filtered according to the GTI via the *gtmktime* function and via *gtselect* which makes cuts based on the time, energy, position, zenith angle, instrument coordinates, event class and event type.

Then a 3-D binned counts map is created for the following binned likelihood analysis. Hereby the data is arranged as a three-dimensional counts map with an energy axis. This so-called counts cube is then used for the optimisation of the starting model to the measured photons. To predict the number of photon counts from the source model, the exposure is computed. For that, the expected photon detection efficiency and the angular

²<https://fermi.gsfc.nasa.gov/cgi-bin/ssc/LAT/LATDataQuery.cgi>

³<https://fermipy.readthedocs.io/en/latest/>

resolution of *Fermi*-LAT are taken into account. To reduce the computational steps of the exposure calculation, the so-called livetime which is the time when the detector is operational and provides valid data is calculated in advance. Afterwards, a model of the region is created and stored as an XML file. The model consists of the 4FGL-DR4, the latest data release version of the 4FGL catalogue, as well as the galactic diffuse emission `gll_iem_v07.fits` and the isotropic emission `iso_P8R3_SOURCE_V3_v1.txt`.

During the optimisation, the sources with their spectral model parameters contained in the model file are fitted to the measured counts. With the logarithm of the likelihood \mathcal{L} , the goodness of the fit is quantified (see the previous section 4.3). Hence, the optimisation corresponds to a maximisation of the likelihood or rather a minimisation of $-\ln \mathcal{L}$, since in computing, the algorithms are optimised for minimisation. After the model was adjusted to the database through four optimisation runs, it was searched for other point sources, which are not in the catalogue, but which are with 5σ significant for the ROI. In most cases the analysis with `find_sources()` did not find an extra source, only for PKS 0454-234 and PKS 2155-304 an extra source was found, each respectively with a distance greater than 2° away from the SMBHB candidate. Hereby, the inner region around the target did not change significantly and no further analysis is needed. In the case when a source was detected and added to the ROI, a second optimisation was performed to readjust the model.

To check the quality of the resulting model, the residual maps are plotted. Those can be seen in the appendix (Figures 1 - 5). The residual map shows the deviation of smoothed data and the model. Consequently, it should not have structured or large residuals as this would hint at a controversy between model and reality. For this analysis, no critical deviations are observed and therefore the fits are accepted.

When a sufficient model was obtained, the LC was computed with a 28-day binning for the whole time interval (shown in Table 5.1). For that, the function `lightcurve()` does sequentially fit the characteristics, like flux and TS, of the target source in time bins. In each time bin, the model will be initialised with the parameters of the sufficient model from before the lightcurve function. Then a selection of parameters will be refitted for each time bin. Those parameters can be chosen through the arguments of the lightcurve function. In this analysis, the background was freed as well as the norm of the spectral model of the target. The high value of `shape_ts_threshold` prevents other sources from being fitted as well because only sources with larger TS values will be freed for refitting. The Python script as well as the `config.yaml` file used for the *Fermi* analysis can be found in GitHub⁴. Furthermore, in the repository, there are the jupyter notebooks for the following Spline detrending, sine fitting and the evaluation of the Doppler-boost hypothesis.

In the case of PKS 0454-234, the residual map showed an overfitting of the target and

⁴<https://github.com/Kilian-3/BA-orbital-Doppler-boosting.git>

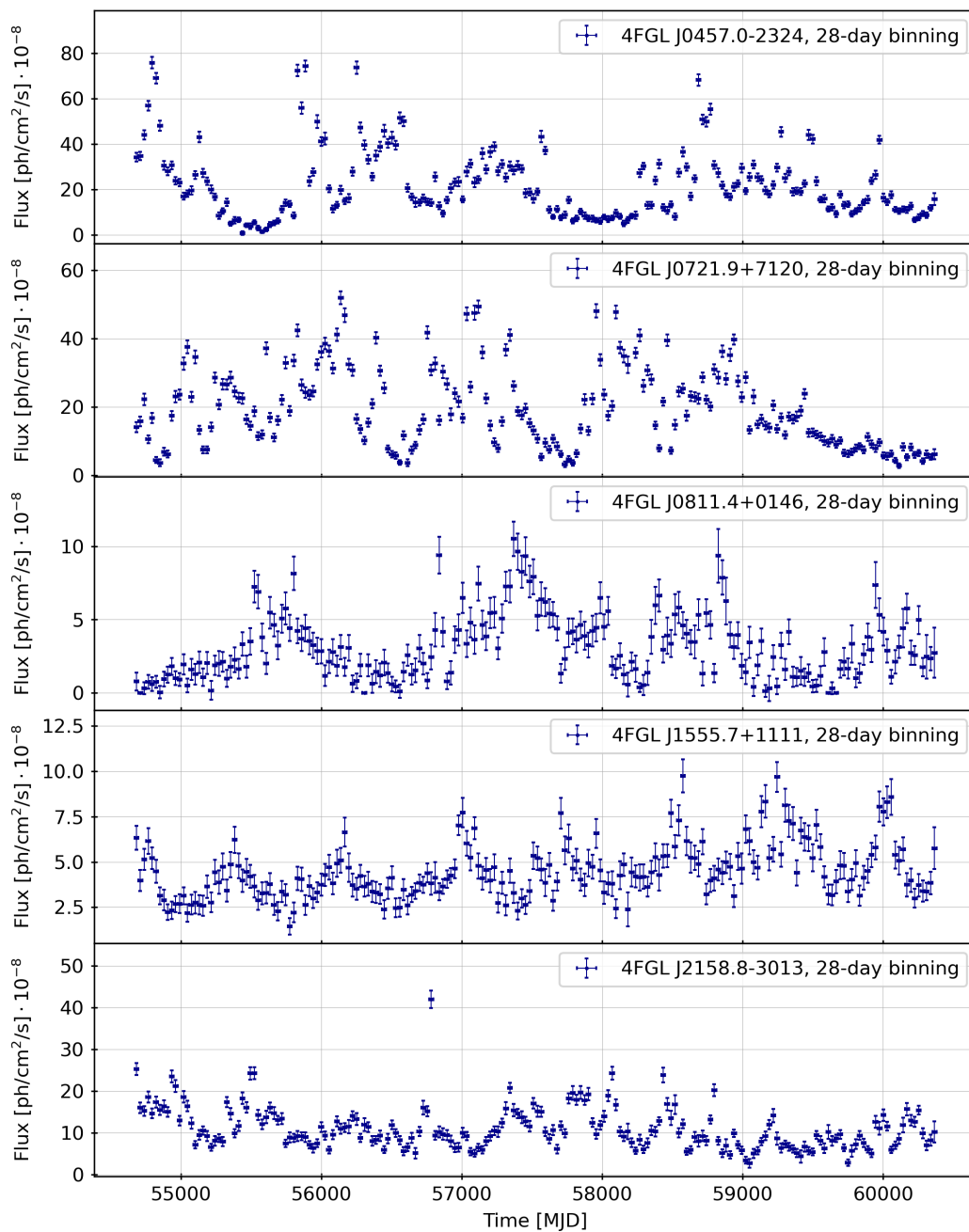


Figure 5.1: For all five sources the obtained LCs from the *Fermi*-LAT analysis are shown. A 28-day binning was commonly used. The flux is depicted in units of photons per area per second [ph/cm²/s].

hence the number of optimisation runs before and after the `find_sources` function was each reduced to one.

5.2.2 Detrending

Apart from the short-term fluctuations in the LCs, there are also long-term trends visible. To cope with those macro-trends the Spline method from De Toma (2022) [18] has been applied. Over the past decades different methods were developed and tested, e.g. Welsh (1999) [56]. One common approach is to fit a polynomial to the data. This method needs according to De Toma (2022) [18] at least $\sim 5 - 10$ cycles for a proper detrending. For OJ 014 with a period of 4.1 yr, this would require 20 years of data, but at the moment only roughly 16 years are available with *Fermi*'s mission launch in 2008. In conclusion, the observational data is too sparse to do a proper detrending with a polynomial fit.

The Spline method, on the other hand, is totally independent of the LC's length and is therefore being used here. It interpolates the trend of some given points as input with a mathematical piecewise polynomial function. In this case, a cubic function was used. The Spline returns a smooth curve that passes all input coordinates. For the detrending, those points are set to the average of a certain amount of data points of the LC. Hence, the input coordinates are equivalent to an under-binned version of the LC. The number of data points combined into an average is referenced in the following as the Spline binning. At the edges, additional points are added to fix the Spline and to make it more robust against changes in the Spline binning. De Toma studied in her master thesis [18] the Spline method and the impact of different Spline binnings on the extraction of a period. For that, she fixed the endpoints to the first and the last data point available. As for this thesis, the period is not extracted from the LC but the amplitude. As a consequence, the Spline should ideally be smooth and follow the mean of the LC. But with a Spline fixed to actual data points themselves at the edges the Spline can in some cases be fixed to a maximum or a minimum and therefore distort the short-term fluctuations and the resulting amplitude from the sine fit. To improve that, in my work, the endpoints were fixed to the mean flux value over half a Spline bin at the edges and their time coordinates were fixed to the limits of the observation interval, the start and the end.

5.2.3 Sine fitting

After the Spline was subtracted from the original LC, the now detrended LC is used to fit a sine with the Python function `scipy.optimize.curve_fit` [57] onto the cleaned data. In a more conservative approach, half of the Spline bin size is excluded for the sine fit at the beginning and at the end of the time interval due to the modifications discussed before. As with this approach, we cannot take into account the entire amount of data available,

a second method was tested. In this additional method, the whole time interval is used for the sine fit and the subsequent amplitude calculation. For all further discussion, this analysis will be referenced as the uncut version since no cut to the data was applied. The goal of the uncut method is to compare the impact of the methodology on the fit result since for the prior analysis only a limited amount of cycles in the LC are available and with more data points the sine fit may change.

Along the detrended data, also the flux errors were given to the curve-fit function to have a more accurate depiction of the data. The outputs of the curve-fit function are both the optimal parameters and the covariance matrix from which the errors of the parameters can be calculated by taking the square root of the diagonalised matrix. The sinusoidal wave used for the curve-fit is a function of the time t (in days) with the form of,

$$f(t) = A \cdot \sin \left(\frac{2\pi}{365.25 \cdot P} t + \phi \right) + C, \quad (5.5)$$

where A is the amplitude, ϕ the phase, C the offset, and P is the period time in years. For the final analysis the period P was fixed on the GLSP period values suggested by Peñil et al. (2022) [16] (see Table 5.4). The other three parameters amplitude, phase and offset were fitted with initial guesses. As for the offset the initial parameter was set to the mean of the fitted data points, the phase was set to an arbitrary number and the amplitude was guessed to be the standard deviation times $\frac{3}{\sqrt{2}}$, which approximates the true amplitude by an upper value. Beforehand, it was checked that with freed periods the sine fit with roughly three years more of data does indeed result in a comparable period as from the GLSP in the paper.

5.2.4 Determination of the best Spline binning

Since with different Spline binnings the Spline curve changes, one has to determine which Spline binning is optimal for the analysis. For this thesis, we are interested in the amplitude of the sinusoidal wave. Therefore, the goal of the detrending is to smooth the LC so that each cycle is roughly on the same level. To assess the goodness of the detrending, the χ^2_{red} was calculated for each sine fit with differing Spline bin detrending. The tested spline bins range from 2 to 100. The equation⁵ used for the χ^2 is,

$$\chi^2 = \sum_i \left(\frac{F_i - f_{opt}(t_i)}{\sigma_{F_i}} \right)^2, \quad (5.6)$$

with the optimal sine fit $f_{opt}(t)$ (see equation 5.5) and the detrended flux values F_i with their respective error σ_{F_i} . To get the reduced χ^2_{red} , the χ^2 was divided by the degrees of

⁵adapted from the documentation from curve-fit:

https://docs.scipy.org/doc/scipy/reference/generated/scipy.optimize.curve_fit.html

freedom, that is the number of data points used for the sine fit minus the three parameters fitted. For the uncut analysis, the χ_{red}^2 was calculated onto the total time interval and for the other method only onto the reduced time interval, on which also the sine fit was performed.

In Figure 5.2, the χ_{red}^2 as well as the resulting amplitude of the sine fit is shown for both methods for the source PG 1553+113 in dependence of the used Spline binning. For the other sources the diagrams are shown in the appendix (see Figures 10 - 13).

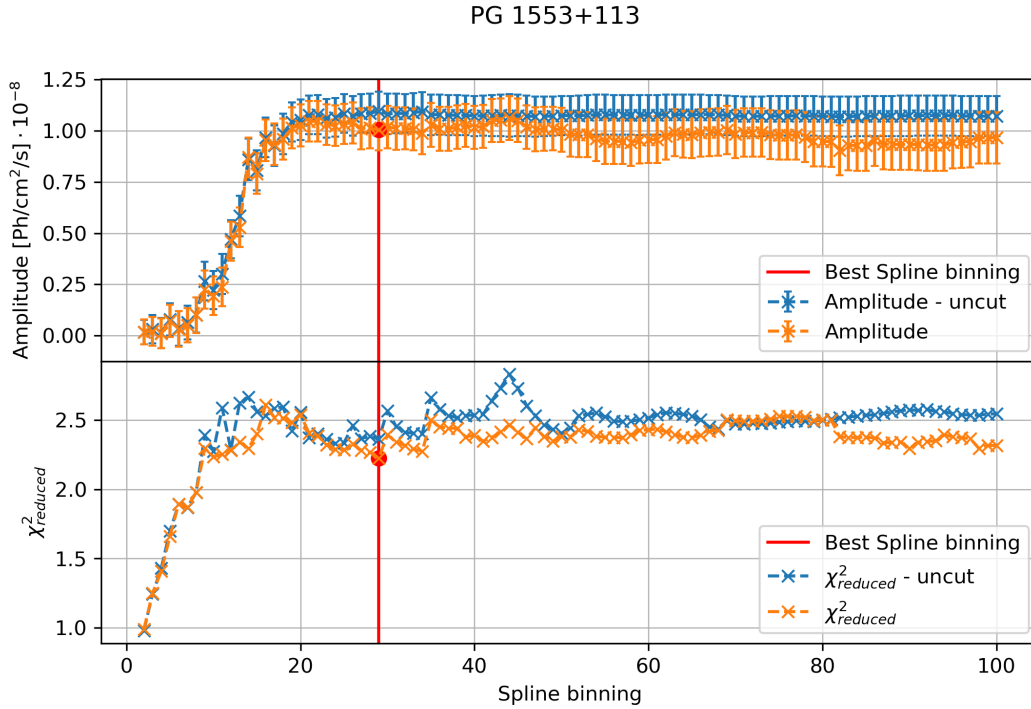


Figure 5.2: In the upper panel, the resulting amplitude from the sine fit is shown for the 2 – 100 tested Spline bins. In the lower panel, the corresponding χ_{red}^2 is shown. The orange line displays the amplitude fit with half a Spline bin excluded at both ends of the time interval. The blue line displays the amplitude fit on the full-time interval. The best Spline binning for the analysis with reduced time interval (stated in Table 5.5) is marked in red.

In most cases, the χ_{red}^2 of the uncut analysis is larger than the counterpart of the more restricted method, especially for OJ 014. For PKS 0454-234 and for S5 0716+714 the χ_{red}^2 of both methods are quite evenly distributed. However, due to the large χ_{red}^2 value, it is of no significance. Therefore, the more restrictive analysis method with reduced time interval will be used in further evaluations.

Note that for low Spline binnings the Spline is overfitting and does not only cope with the macro-trend but also for the year-long oscillations we want to analyse. Hence, for small Spline bins, the LC gets flattened and the amplitude diminishes. To prevent overfitting, the minimal Spline bin was determined with the amplitude evolution seen in the diagram.

For each source, the Spline bin was estimated where the rising amplitude goes over to a constant level. This means that the value of the amplitude is not depending on the specific spline bins any further. The resulting minimal Spline bins are listed in Table 5.5.

Source	χ_{red}^2 range	Minimal Spline bin	Best Spline bin (χ_{red}^2)
PKS 0454-234	30 - 80	24	24 (41.23)
S5 0716+714	35 - 75	22	22 (55.35)
OJ 014	3 - 7	30 / 32	39 (3.62)
PG 1553+113	2.2 - 2.9	16 / 20	29 (2.23)
PKS 2155-304	9 - 14	15	21 (9.75)

Table 5.5: Determination of the best Spline binning for the amplitude analysis with reduced time interval. The two columns about the χ_{red}^2 range and the minimal Spline binning are being used for the evaluation of the best Spline bin.

Furthermore, the range of the χ_{red}^2 over the different Spline binnings is stated there. For PKS 0454-234 and for S5 0716+714 the χ_{red}^2 is too large to have any significance and is therefore not taken into account, thus the minimal Spline bin was used.

For the other three sources, the χ_{red}^2 can be used to further determine the best Spline binning. A χ_{red}^2 around 1 indicates the best accordance between the fit and observation, while $\chi_{red}^2 > 1$ hints at a discrepancy between those. Consequently, the Spline binning with the smallest χ_{red}^2 among the Spline bins that are larger than the minimal Spline bin was selected for the analysis.

Furthermore, care was also taken to ensure the smallest possible Spline bin was being used as to minimise the neglected data points due to the cut at the edges based on the Spline method. As this cut is proportional to the Spline binning, a lower Spline bin is preferable. That is also the reason, why the minimal Spline bin was used for the sources with too high χ_{red}^2 . In the last column of Table 5.5, the optimal Spline binnings according to these criteria are written. Those will be used in the further analysis.

In Figure 5.3 as well as in Figures 6 - 9 in the appendix, both the Spline detrending and the sine fitting are shown for the best Spline binning determined in this section. In each case, the original LC and the Spline are depicted in the upper panel and in the lower panel the detrended LC as well the sine resulting from the curve-fit is shown. In the latter, it is noticeable that for larger photon fluxes there is a greater deviation from the sinusoidal wave. Those systematic peaks are due to the effect of logarithmic scaling in the emission, which causes the fluctuations to scale logarithmically with higher fluxes.

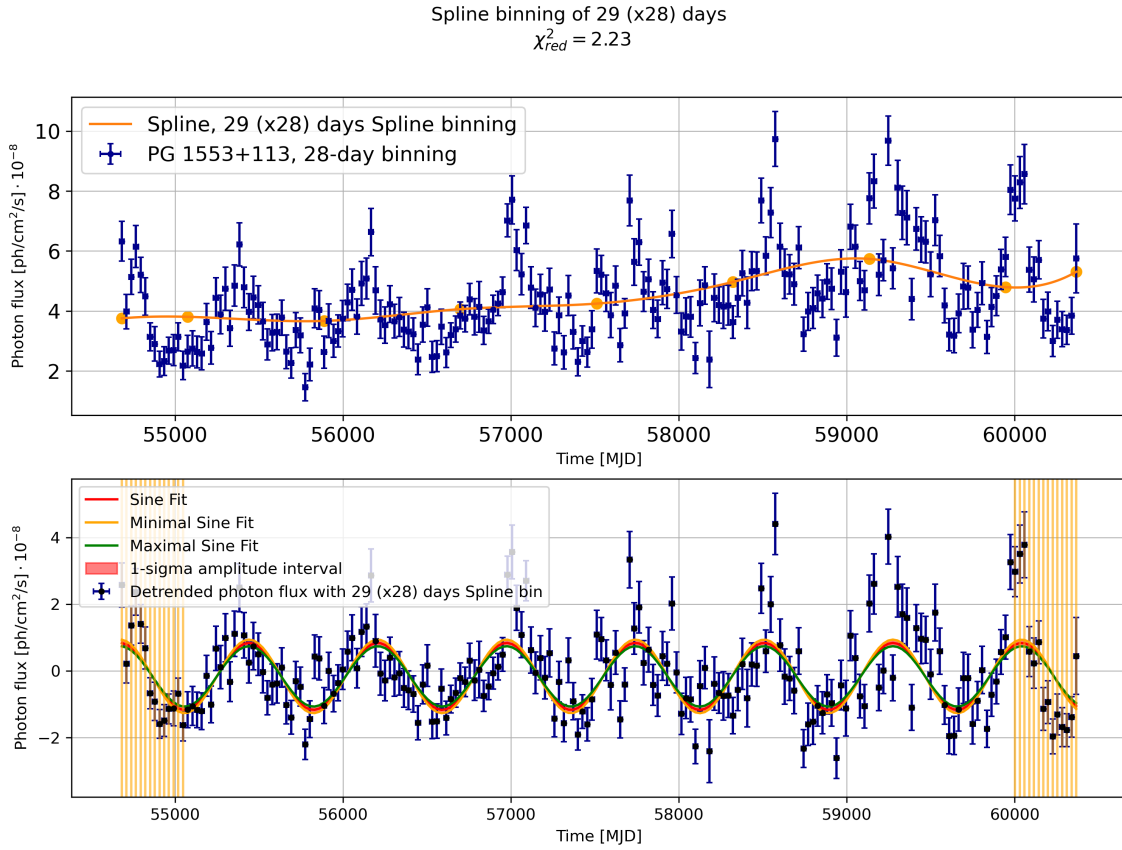


Figure 5.3: In this figure, the Spline detrending as well as the sine fitting is shown for PG 1553+113. The best Spline as well as the original LC are plotted in the upper panel. For the Spline binning, the value determined in section 5.2.4 was used for the optimal detrending. In the lower panel, the detrended LC and the sine fit are shown. Furthermore, the 1- σ -band is plotted between the sinusoidal waves with amplitudes plus (minus) the error of the amplitude. The vertical bars at the edges of the time interval mark the excluded data points for the sine fit due to the endpoints of the Spline.

Chapter 6

Evaluation of the Doppler-boost hypothesis

According to Charisi et al. (2018) [58], the amplitude required for equation 3.17 is defined as

$$A = \frac{\Delta F}{F_{mean}}, \quad (6.1)$$

where ΔF is the amplitude found by the sine fit and F_{mean} is the averaged flux of the original LC in the time interval of the sine fit. The error calculation was done according to Gaussian error propagation [44],

$$\sigma_A = \frac{\Delta F}{F_{mean}} \sqrt{\frac{\sigma_{\Delta F}^2}{\Delta F^2} + \frac{\sigma_{F_{mean}}^2}{F_{mean}^2}}. \quad (6.2)$$

The resulting amplitudes used for equation 3.17 are listed in Table 6.1 where ΔF and F_{mean} are obtained through the analysis described in the previous chapter.

sources	amplitude
PKS 0454-234	0.434 ± 0.061
S5 0716+714	0.368 ± 0.060
OJ 014	0.610 ± 0.068
PG 1553+113	0.242 ± 0.024
PKS 2155-304	0.229 ± 0.037

Table 6.1: Amplitudes derived from the equation 6.1 with the given ΔF from the sine fit and the averaged flux over the corresponding time interval.

To get the limits of the four unknown parameters (binary mass ratio q , Inclination I , jet velocity β_{jet} and jet direction θ) the derived equation 3.17 gets solved for each of them. One obtains:

$$q = \frac{\sin I}{A \cdot C} [1 + (2 + \alpha_\nu) \beta_{jet} \cos \theta] - 1, \quad (6.3)$$

$$I = \arcsin \left(\frac{A C (1 + q)}{1 + (2 + \alpha_\nu) \beta_{jet} \cos \theta} \right), \quad (6.4)$$

$$\beta_{jet} = \frac{1}{(2 + \alpha_\nu) \cos \theta} \left(\frac{A C (1 + q)}{\sin I} - 1 \right), \quad (6.5)$$

$$\theta = \arccos \left[\frac{1}{(2 + \alpha_\nu) \beta_{jet}} \left(\frac{A C (1 + q)}{\sin I} - 1 \right) \right], \quad (6.6)$$

with $C = \left(\frac{P_{obs}}{2\pi G M (1+z)} \right)^{\frac{1}{3}} \cdot c$.

Each parameter has an initial constrained range due to the model and logical considerations. Those are listed in Table 6.2.

Parameter	Minimum	Maximum
Inclination	0°	90°
Binary mass ratio	0	1
Lorentz factor	1	100
β_{jet}	0	~ 1.00
θ	0°	90°

Table 6.2: Constraints of the parameters due to symmetry, morphological considerations and physical reasons. The inclination I is the angle that the orbital plane encloses with the plane of the sky. The binary mass ratio is defined as $q = M_2/M_1$ with the masses M_1 (M_2) of the bigger (smaller) SMBH. The Lorentz factor, which is related to β_{jet} (see eq. 6.7), describes the blob velocity inside the jet. θ is defined as the angle, which the jet encloses with the line of sight. A more detailed instruction of the model parameters can be found in chapter 3.

According to the model (described in chapter 3), the inclination can be constrained to $[0^\circ, 90^\circ]$ since all other configurations can be devolved into this range due to symmetry and the independent definition of θ . For the angle θ , which the jet encloses with the direction towards Earth, one can use the common knowledge that jets always come in pairs. Therefore, when one points away from Earth, the other one faces towards us. And, since the jet emission is Doppler boosted, the one facing Earth will dominate the emission.

I_{max} [°]	q_{min}	$\beta_{jet,max}$	γ_{max}	θ_{min} [°]
90	0	~ 1.00	100	0

Table 6.3: Upper or lower limits of the different parameters in the optimal Doppler-boosting case. Those general limits can be applied to all sources.

Hence, θ can be restricted to $[-90^\circ, 90^\circ]$. Furthermore, when considering also the radial symmetry of the system, the angle θ can be fixed to $[0^\circ, 90^\circ]$. Note that all five sources of the test sample are blazars and have a jet closely aligned to our line of sight. Therefore, θ should be ideally fixed to a lower value, but to keep it general, the full range has been used. The binary mass ratio is by definition positive and ≤ 1 . The same applies to β_{jet} . Since we are dealing with a jet, β_{jet} can be further constrained by the upper bound of 100 of the Lorentz factor γ for jets, which is commonly used to describe near relativistic speeds. With the relation

$$\gamma = \frac{1}{\sqrt{1 - \beta^2}} \quad \Longleftrightarrow \quad \beta = \sqrt{1 - \gamma^{-2}}, \quad (6.7)$$

this upper bound can be converted into an upper bound of β_{jet} .

Using those plausible parameter ranges, one can plot each possible parameter with given values from the other three variables. The resulting diagrams are shown in Figure 6.1 for the source PG 1553+113 and in Figure 6.2 for PKS 2155-304. To visualise the dependence of the four parameters, the inclination, the binary mass ratio and the angle θ were plotted against increasing jet velocities in each row. For a whole depiction of the dependence, β_{jet} started slightly below the threshold, where Doppler boosting was possible. Hence, the first row depicts blank diagrams. For the other sources, all the diagrams were blank since no set of parameters could be found that fulfilled equation 3.17 (the reason behind that will be discussed in the following chapter 7). In the figures, one can see the radial symmetry of the jet direction, since θ was plotted from -90° to 90° .

To provide some quantitative limits, a secondary calculation was performed. To get the limits, found by the analysis, of each parameter, they are computed according to the equations 6.3 - 6.6, respectively, with the other parameters fixed to the optimal Doppler-boosting case. In the optimal Doppler-boosting case, the inclination is 90° , hence maximal, the smaller SMBH mass is negligible compared to the larger SMBH ($q \simeq 0$) and the jet faces straight towards Earth with the highest possible blob velocity ($\theta = 0^\circ$ & $\gamma = 100$), thus forming the one side of our limits (see Table 6.3). The found other upper or lower limits depending on the parameter for each source are stated in Table 6.4.

When both lower and upper limits span a reasonable range, meaning the upper boundary is greater than the lower one, the Doppler-boost hypothesis is feasible and otherwise not. In the case of PG 1553+113 and PKS 2155-304, the range was reasonable and thus the

observed variability can be explained by the orbital Doppler boosting.

Sources	I_{min} [°]	q_{max}	$\beta_{jet,min}$	γ_{min}	θ_{max} [°]
PG 1553+113	22.3 ± 7.6	1.64 ± 0.86	0.20 ± 0.16	1.022 ± 0.034	78.2 ± 9.2
PKS 2155-304	36 ± 14	0.69 ± 0.59	0.48 ± 0.26	1.14 ± 0.19	61 ± 17

Table 6.4: Found upper or lower limits through the analysis. Together with the limits from Table 6.3, they form the possible parameter range in which the Doppler-boost hypothesis is viable.

For the other three sources, the upper or lower limits crossed the other ones defined in Table 6.3. As a result, the Doppler-boost hypothesis is rejected. To get an understanding of the significance of their mismatch with the Doppler-boost hypothesis, the found upper limit of the binary mass ratio q_{max} is given in Table 6.5. Physically meaningful would be a $q_{max} > q_{min} \simeq 0$.

Sources	q_{max}	Deviation from $q_{min} \simeq 0$ [σ]
PKS 0454-234	-0.42 ± 0.11	3.8
S5 0716+714	-0.48 ± 0.18	2.7
OJ 014	-0.47 ± 0.29	1.6

Table 6.5: Found upper limits through the analysis for the binary mass ratio. To accept the Doppler-boost hypothesis, q_{max} should be greater than $q_{min} \simeq 0$.

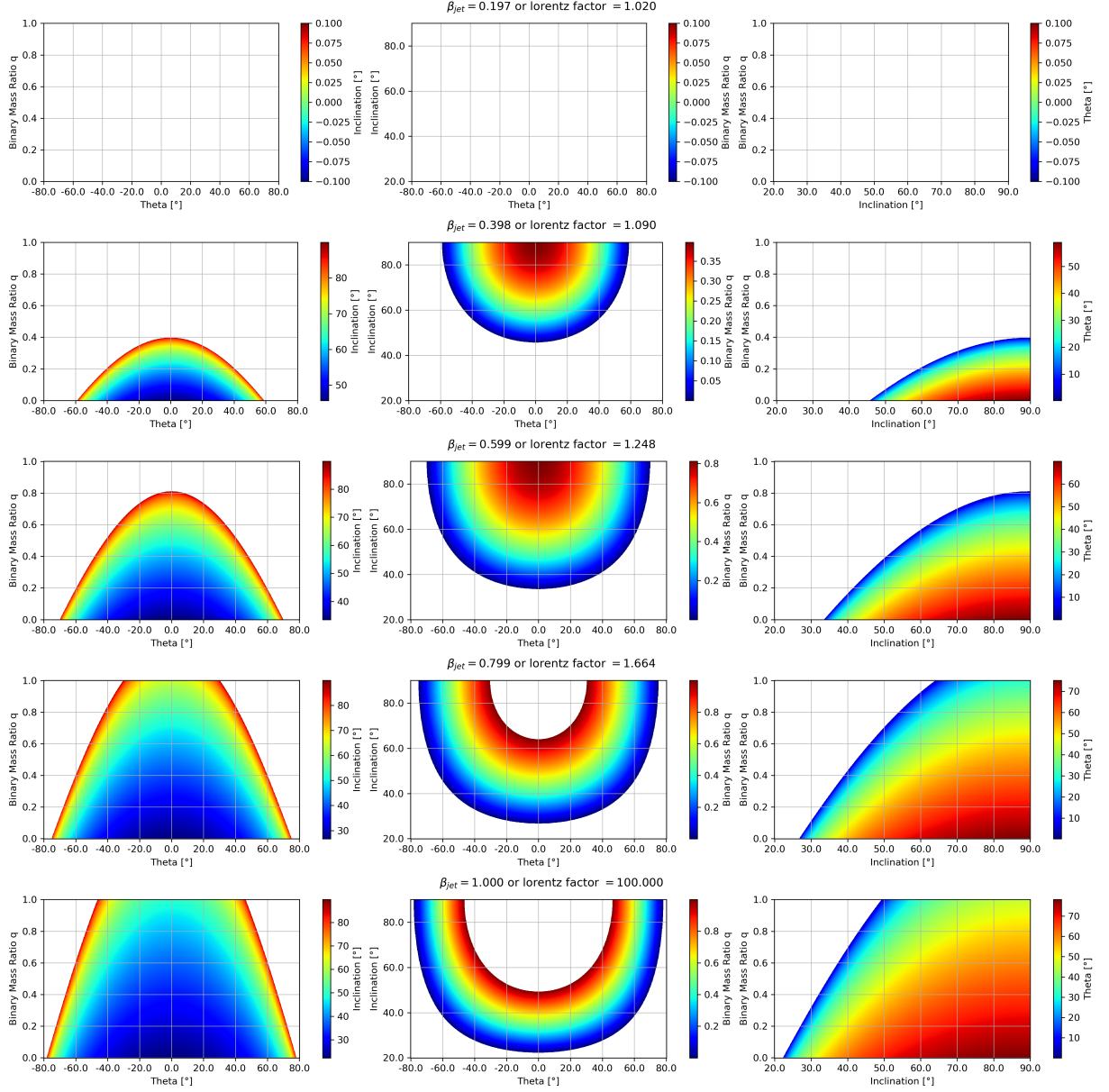


Figure 6.1: Possible sets of parameters for PG 1553+113, for which the Doppler-boost hypothesis is viable. In each row, the dependence of the three parameters inclination, binary mass ratio and the angle θ is shown with increasing β_{jet} .

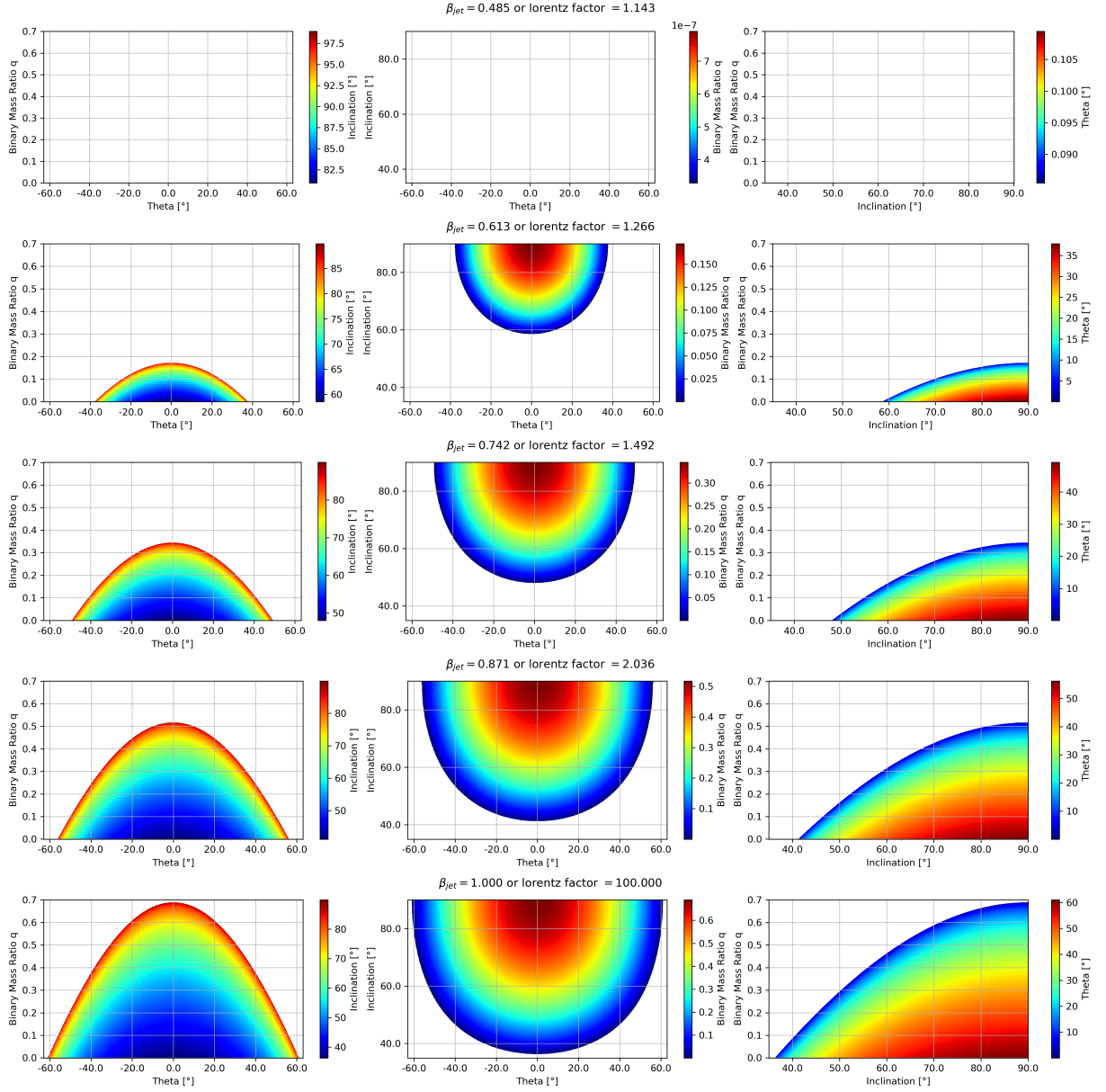


Figure 6.2: Possible sets of parameters for PKS 2155-304, for which the Doppler-boost hypothesis is viable. In each row, the dependence of the three parameters inclination, binary mass ratio and the angle θ is shown with increasing β_{jet} .

As one can see in Figure 6.1, the possible parameter space in the optimal Doppler case is limited by the binary mass ratio to $q \leq 1$. The fit results on the other hand, which give a $q > 1$, can be explained with a Doppler Boosting solely produced from the larger SMBH. In this model, the smaller SMBH has no jet and hence, does not contribute to the observed luminosity in the gamma-ray band. The equations were changed according to the different orbital velocities (see equations 3.10 and 3.11). For the more massive SMBH in the binary, the Doppler effect theory would be viable only for PG 1553+113. The possible sets of parameters are shown in Figure 6.3. For better comparison, the axes have the same scale as the previous diagrams for PG 1553+113, shown in Figure 6.1. Only a higher initial β_{jet} was chosen to convey more information because otherwise three of the five rows would depict empty diagrams.

For PKS 2155-304, the scenario, in which the Doppler-boost hypothesis is based on the more massive SMBH, is not feasible and the corresponding minimum binary mass ratio would be $q_{min} = 1.45 \pm 0.28 > q_{max} = 1$. The limits for PG 1553+113 in this other scenario are listed in Table 6.6. Similar to the previous calculated limits, each bound was calculated with the other parameters fixed to the value from the optimal Doppler boost. For the Doppler boosting from the more massive SMBH, apart from the binary mass ratio, all other parameters are in the optimum case the same as for the smaller SMBH. But to achieve the highest Doppler boost, q has to be maximal as opposed to the case near 0 from the smaller SMBH because in this case, the orbital velocity of the emitting SMBH is maximal.

Sources	I_{min} [°]	q_{min}	$\beta_{jet,min}$	γ_{min}	θ_{max} [°]
PG 1553+113	49 ± 22	0.6 ± 2.3	0.69 ± 0.31	1.38 ± 0.57	46 ± 25

Table 6.6: Found limits through the analysis for the Doppler Boosting case of the more massive SMBH. Together with the limits from Table 6.3 with $q_{max} = 1$ instead of q_{min} , they form the possible parameter range in which Doppler boosting is viable.

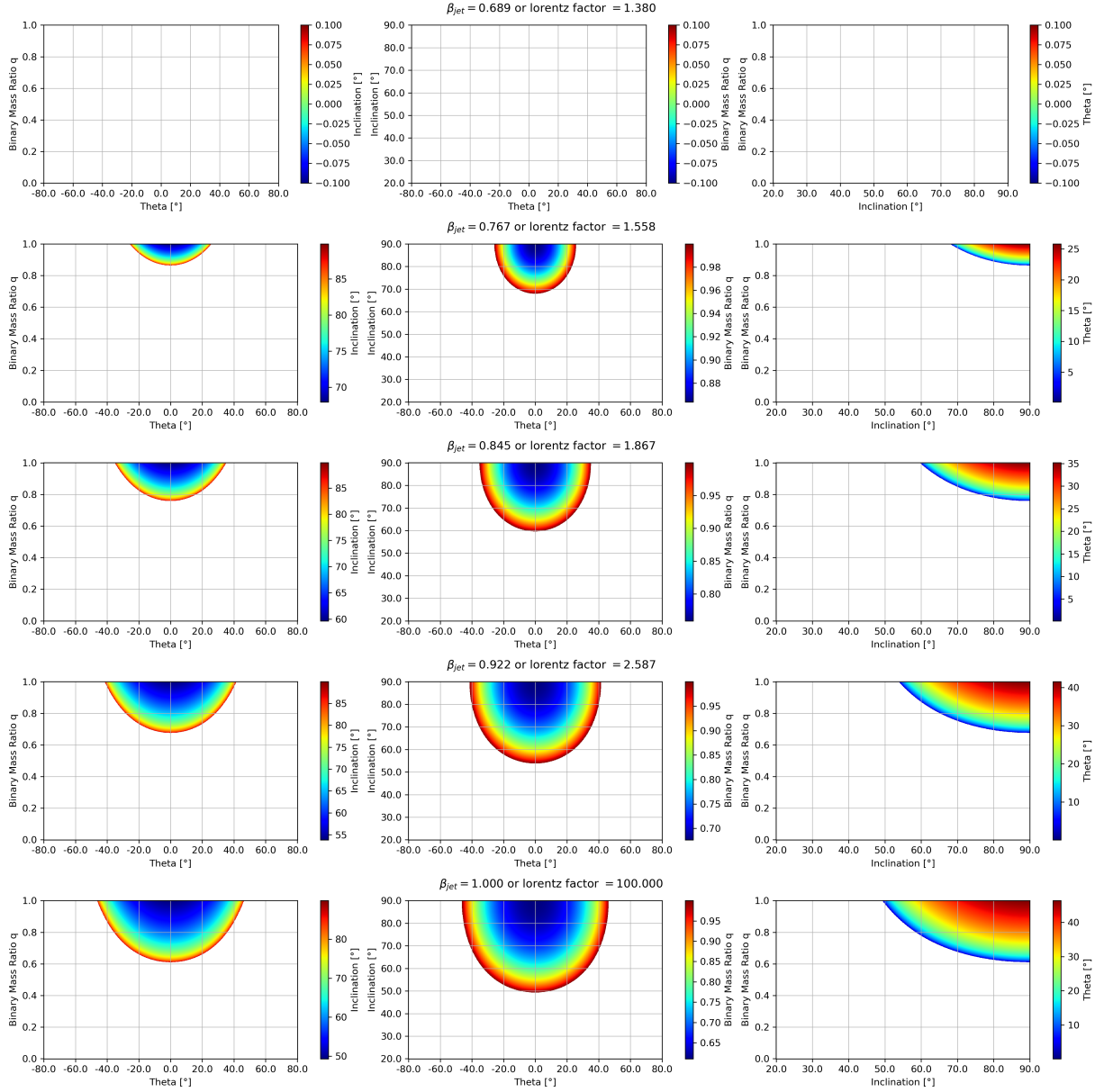


Figure 6.3: Possible parameter space, for which the variability can be explained by Doppler boosting, for PG 1553+113 with the more massive SMBH as the only jetted SMBH which gets Doppler boosted. In each row, the dependence of the three parameters inclination, binary mass ratio and the angle θ is shown with increasing β_{jet} .

Chapter 7

Discussion and Conclusions

The results presented in the previous chapter show that for PG 1553+113 and for PKS 2155-304 the Doppler-boost hypothesis may be a viable explanation for the observed periodic behaviour. On the hand, for OJ 014, PKS 0454-234 and S5 0716+714 the Doppler-boost hypothesis is not a viable solution. One reason for that could be the relatively high amplitude compared to the other sources (see Table 6.1). To compensate for the high value on the one side of the equation 3.17, one would need either small period times or large SMBHB masses, redshifts or spectral indices. For these sources, neither of that is the case. OJ 014 with (4.1 ± 0.4) yr and PKS 0454-234 with (3.5 ± 0.4) yr have the longest period times observed from the whole sample. Therefore, the Doppler-boost hypothesis cannot explain solely the variability of these sources. Note that for S5 0716+714 apart from the others the redshift could not be measured and was therefore estimated by an upper limit. This makes the hypothesis even more unlikely because the limits were calculated using the upper limit and it can be assumed that the actual redshift is lower. Going back to the evaluation of the goodness of the fit in section 5.2.4, it was seen that for the sources PKS 0454-234 and S5 0716+714 the χ^2_{red} was too high to ensure a reliable fit. The χ^2_{red} quantifies how well the model describes the data. So for those two sources, when the value is high, it could mean that the sinusoidal wave suggested by the Doppler-boost hypothesis is the wrong model to describe the variability observed in the LC. Since, whenever we are dealing with SMBHB, orbital Doppler boosting generally applies, a possibility could be that the orbital Doppler boosting is supplementing another more dominant phenomenon causing the variability.

Another interesting fact is that the variability of S5 0716+714 decreased drastically in the past years (see Figure 5.1). This could hint at a change in the astrophysical nature of the AGN. Alternatively, also random processes mimicking periodicity for a few cycles could be taken into account to explain the variability before this change. For this, a more sophisticated study has to be done in order to understand this change better. For example, one could use the *spectral energy distribution* (SED) before and after this switch

to determine the radiative components of the AGN. But this will not be discussed any further since it is beyond the scope of this thesis.

The results from the previous chapter show that for PG 1553+113 as well as for PKS 2155-304 orbital Doppler boosting can explain the observed flux variability in the gamma-ray-regime. For both sources, the parameter ranges of the jet angle θ and its Lorentz factor are well inside the morphological boundaries of a blazar, which according to its definition (see section 2.2) has a relativistic jet closely aligned to the line of sight, i.e. a small θ and Lorentz factor > 1 . The binary mass ratio q of PKS 2155-304 can range from very small values up to 0.69 ± 0.59 , where the two SMBH are roughly of the same order of magnitude.

According to the analysis, the SMBHB of PKS 2155-304 orbits with a minimum inclination of $(36 \pm 14)^\circ$. This could be realistic because through friction lower inclinations of the orbital plane compared to the rotational plane of the host galaxy are preferred.

Note that the inclination limits derived in this analysis are with respect to the plane of the sky and not to the accretion disk. But, since we are dealing with blazars and it can be assumed that the jet faces perpendicular to the main accretion disk, the plane of the sky can be treated equally as the plane of the accretion disk.

The same applies for PG 1553+113. With a lower limit of $(21.9 \pm 7.5)^\circ$ to the inclination, the Doppler-boosting hypothesis is even more preferable than in the other source. But unlike the other one, the found maximum mass ratio exceeds 1 and hints at the possible Doppler-boost hypothesis, where the emitting jet is connected to the more massive SMBH instead of the smaller one. This has been tested. The results of the testing showed that for PG 1553+113 it is possible whereas for PKS 2155-304, it is not. Hence, the observed variability of PG 1553+113 can be interpreted to originate from Doppler boosting from the jet of the smaller SMBH or, in the case of higher inclinations and relatively similar SMBH masses ($0.6 \leq q \leq 1$), from Doppler boosting from the jet attached to one of the two SMBHs (see Table 6.6).

Next, we will discuss the caveats in the analysis method itself. Beginning with the derivation of the Doppler equation used for this analysis, it should be noted that the modelling of the jet is quite simplified. It is assumed that the jet does not deform while its origin, i.e. the SMBH which orbits around the centre of mass, moves around. Furthermore, the angle θ which the jet encloses with the line of sight is time-independent, meaning the jet does not rotate along the orbital motion (apart from the special case where the jet rotation does not change θ due to radial symmetry with respect to the line of sight). Another point is the assumption of a circular orbit used for the derivation of β_{jet} in equation 3.6. According to Rieger (2006) [59] dynamical friction together with accretion disk interactions and gravitational radiation can form nearly circular orbits. However, for a more detailed analysis, a more general derivation of an elliptic orbit should be done in the future.

Proceeding with the detrending, we introduced a method to determine the best Spline binning for the amplitude analysis. The advantage of the Spline method is that the detrending is independent of the length of the LC. On the contrary, half a Spline binning on both ends of the time interval had not been taken into account in the following analysis of the detrending due to the additional fix points at the ends. So for future analyses, the Spline method should be more investigated to improve the determination of the Spline binning and the handling of the boundaries. Alternatively, when the observation time is sufficient, the polynomial detrending could be applied.

Finally, in the testing of the Doppler-boost hypothesis, it should be noted that the total SMBHB mass estimates can have a significant impact on the results. For example for PG 1553+113 with the masses assumed in Tavani (2018) [20] of $M_1 = 5 \times 10^8 M_\odot$ and $M_2 = 5 \times 10^7 M_\odot$ the hypothesis would not be viable that the variability is coming from the Doppler boost of the more massive SMBH's jet whereas with the more recent estimate from Chen et al. (2024) [47] it is viable.

Chapter 8

Future perspectives

In future applications of the Doppler-boost hypothesis, it would be interesting to study the variability of photon emission above 1 GeV because, in this energy range, the sinusoidal wave is more pronounced whereas in the lower gamma rays, other fluctuations are more present (Larsson priv. comm.). In addition, the Doppler-boost hypothesis could be extended such that it accounts not only for Doppler boosting from one jet but for both possible existing jets of the two SMBHs. With the current equation, this change would introduce three additional variables (flux, jet velocity and jet angle of the second jet) with the assumption of equal spectral indices of both jets. As a consequence, a more sophisticated theoretical study of the SMBHB to reduce the free parameters and to find correlations between them would benefit the analysis a lot.

Furthermore, one could improve the hypothesis by generalising the derivation of β_{orb} from a circular orbit to an elliptic one and also treating the whole system according to general relativity. Additionally, as explained in section 5.2.4, the fluctuations in the flux scale are logarithmic. Therefore, an analysis was performed in the Log scale, with no improvements. Maybe in future works, the phenomenon of logarithmic scaling fluctuations can be addressed in a more suited way.

From a more theoretical standpoint, it would be interesting to compare different derivations of the orbital Doppler boosting. This work was based on the derivation of D’Orazio and Charisi (2023) [1]. Next to this also Rieger (2004) [21] and O’Neill (2022) [60] did each their own derivation of the orbital Doppler boost phenomenon with different outcomes.

Finally, Doppler boosting should appear in all emitted wavebands. Therefore, a study of the whole spectrum would give us a more complete picture of the AGN. In the recent study of the *Magic* Collaboration H. Abe et al. (2024) [61], this was partially done for PG 1553+113 where they compared the variability patterns from different wavebands. The next step would be to interpret those variability patterns with the Doppler-boosting hypothesis (similar to what has been done in Rieger (2007) [23] with a combination of different theories).

Chapter 9

Summary

In this work, the variability of five sources in the gamma ray was studied regarding the question of whether or not it could be explained by orbital Doppler boosting of the jet emission from one of the SMBHs. In the beginning, a gamma-ray data analysis was performed to get the LCs of each source in the sample. Then a Spline detrending was done respectively to cope with the macro-trend present in the LCs. The goal of which was to remove the red noise component. Due to the fixed points at the edges of the time interval, two analysis methods were introduced. The so-called uncut version would include the total time interval in further analysis steps and the other one would exclude half a Spline bin each at both ends. With the method developed to determine the best Spline binning for the detrending, it additionally showed which of the two analysis versions was better. As a result, the uncut version was neglected and the more restrictive one where half a Spline bin was excluded was used for further analysis. After the detrending, a sine was fitted onto the detrended LC and the resulting amplitude was used for the evaluation of the Doppler-boost hypothesis. The outcome of this evaluation was that the Doppler-boost hypothesis is only viable for PG 1553+113 and PKS 2155-304. With found minimum inclinations of $(21.9 \pm 7.5)^\circ$ and $(36 \pm 14)^\circ$, respectively, the proposed binary system of SMBH in said AGN is realistic. For PG 1553+113 the variability can be even explained by Doppler boosting of the jet connected to the more massive SMBH. For that to happen, the binary mass ratio must be greater than 0.6 and the inclination of the orbital plane with respect to the plane of the sky has to be larger than $(49 \pm 22)^\circ$. Compared to the first Doppler-boost hypothesis connected to the smaller SMBH the latter seems less likely with higher minimum inclination angles but it should be noted that a jet is more likely to emerge from the more massive SMBH than the smaller one. Therefore, the latter hypothesis is also a reasonable model of the AGN.

For the other three sources PKS 0454-234, S5 0716+714 and OJ 014 the Doppler-boost hypothesis was not viable. The first two sources show not only large deviations from the Doppler-boosting case, but also have the highest χ^2_{red} -values of the sine fit with differing

Spline bin detrendings ranging from around 30 and upwards. This indicates that other more dominant phenomena must be taken into account to explain the observed variability. Note that OJ 014 has reasonable χ^2_{red} -values and is also the most likely among the three sources to host Doppler boosting with the smallest deviation among the three of around 1.6σ from the Doppler-boosting case. So it should still be considered in future works. For upcoming studies, we suggest analyses of photon fluxes above 1 GeV because the sinusoid is more pronounced there as well as an extension of the Doppler-boost equation to account also for a second jet, an elliptic orbit and general relativity. Finally, it would be interesting to implement the orbital Doppler boosting hypothesis to different wavebands and to do a multi-wavelength analysis on prime candidates.

Acknowledgement

First, I want to thank my supervisor Professor Sara Buson for her constant support. Even when she is abroad, she always keeps us Bachelor students in mind. I am grateful for the very friendly and supportive group environment she has created. She also encourages us to speak with other researchers in the field and enables us to talk with them. Thank you very much for all that!

I also have to thank Leonard Pfeiffer, my inofficial "supervisor" at the desk beside me. He always had time for me and helped me a lot in the preparation of this manuscript, be it in theoretical or practical questions.

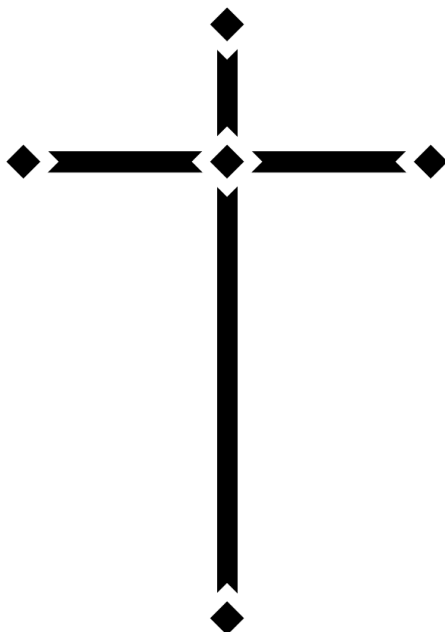
I thank also Margherita De Toma who kindly provided me her script of the Spline De-trending and furthermore explained me the basic concept of it. In the following days, she was always open to questions.

I also want to thank Alessandra Azzollini who helped me in the research of the total SMBHB masses as well as the redshifts. She kindly provided me with citation lists and checked other papers which I found. I am very grateful for this support because the search for such values is very tedious and without knowledge of optical wavelength measurements, it is very easy to get lost.

A particular mention goes to Gaëtan Fichet de Clairfontaine who helped me get started with the derivation of the Doppler-boost hypothesis. Since in gamma rays the equation from the previous paper did not apply, we had to think of another one.

Moreover, I like to thank Margot Boughelilba another theoretician for her support and the final check of my equations.

Lastly, I want to thank the other group members for sharing ideas and feedback in weekly meetings and spontaneous breakout sessions as well as for the nice conversations on a daily basis.



A big thank you to all the proofreaders (namely Sara Buson, Leonard Pfeiffer, Daniel Seifried and Christiane Stein) for their time, ideas for improvement and amusing comments which made my day.

This work was supported by the European Research Council, ERC Starting grant *MessMapp* under contract no. 949555.

Außerdem will ich meiner Familie, insbesondere meinen Eltern, danken, dass sie mir immer als Rückzugsort zur Verfügung standen. Nicht nur die Wochenenden zuhause, sondern auch die (zumal längeren) Telefongespräche haben mich immer wieder aufgebaut.

Und schließlich will ich mich auch ganz herzlich bei GOTT bedanken, der allezeit über mich wacht und mir in den vergangenen vier Monaten in Momenten der Überforderung, der Nervosität und der Verzweiflung (wenn mal wieder alles zu zerbröckeln schien, weil irgend eine Annahme falsch war...) beistand und auch in Zukunft immer beistehen wird.

GOTT sei gepriesen.

Hallelujah!

Appendix

Source parameters for the FSSC data download

Equatorial coordinates (degrees)	(74.2632,-23.4145)
Time range (MET)	(239557417,731505868)
Time range (Gregorian)	(2008-08-04 15:43:36,2024-03-07 12:04:23)
Energy range (MeV)	(100,300000)
Search radius (degrees)	16

Table 1: PKS 0454-234 or 4FGL J0457.0-2324

Equatorial coordinates (degrees)	(110.473,71.3434)
Time range (MET)	(239557417,731505868)
Time range (Gregorian)	(2008-08-04 15:43:36,2024-03-07 12:04:23)
Energy range (MeV)	(100,300000)
Search radius (degrees)	16

Table 2: S5 0716+714 or 4FGL J0721.9+7120

Equatorial coordinates (degrees)	(122.861, 1.78117)
Time range (MET)	(239557417, 731499937)
Time range (Gregorian)	(2008-08-04 15:43:36, 2024-03-07 10:25:32)
Energy range (MeV)	(100, 300000)
Search radius (degrees)	16

Table 3: OJ 014 or 4FGL J0811.4+0146

Equatorial coordinates (degrees)	(238.929,11.1901)
Time range (MET)	(239557417,731505868)
Time range (Gregorian)	(2008-08-04 15:43:36,2024-03-07 12:04:23)
Energy range (MeV)	(100,300000)
Search radius (degrees)	16

Table 4: PG 1553+113 or 4FGL J1555.7+1111

Equatorial coordinates (degrees)	(329.717,-30.2256)
Time range (MET)	(239557417,731505868)
Time range (Gregorian)	(2008-08-04 15:43:36,2024-03-07 12:04:23)
Energy range (MeV)	(100,300000)
Search radius (degrees)	16

Table 5: PKS 2155-304 or 4FGL J2158.8-3013

Residual maps

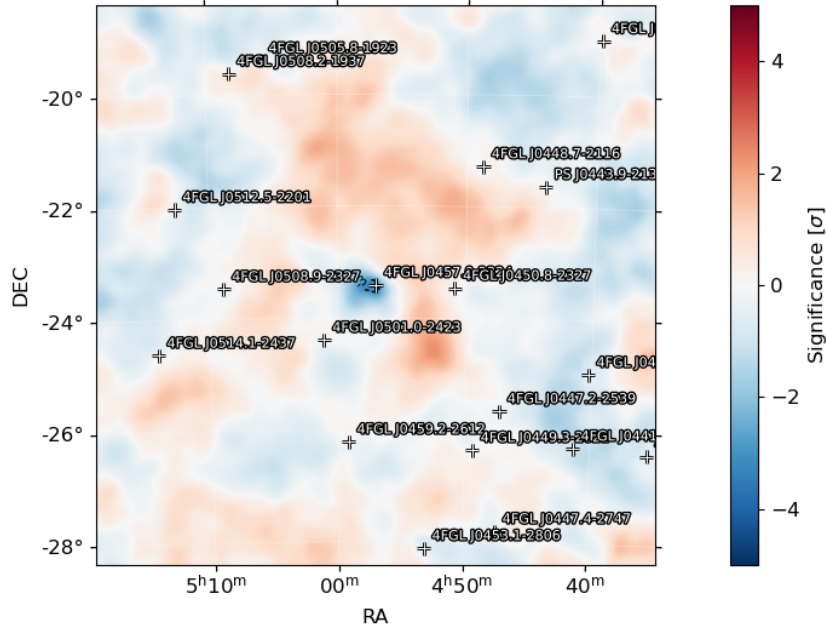


Figure 1: Residual map of PKS 0454-234.

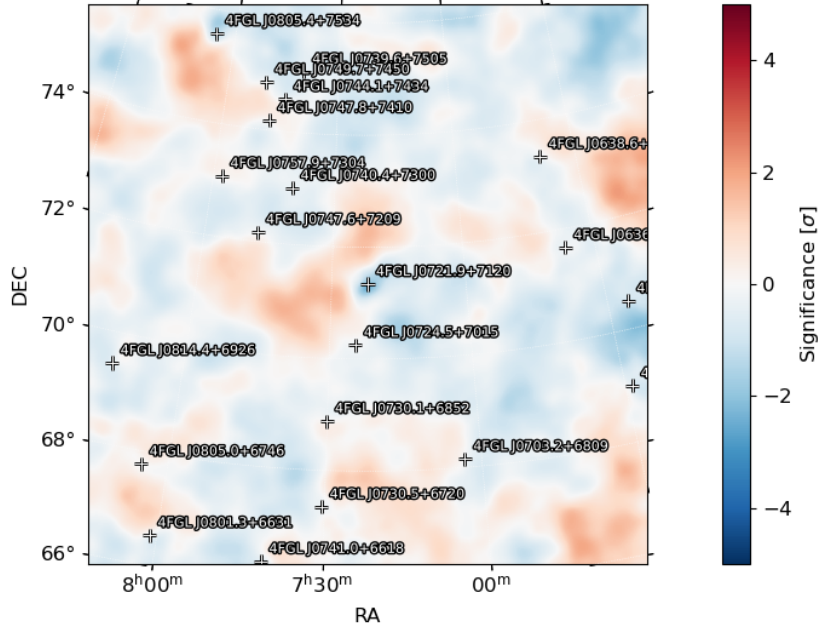


Figure 2: Residual map of S5 0716+714.

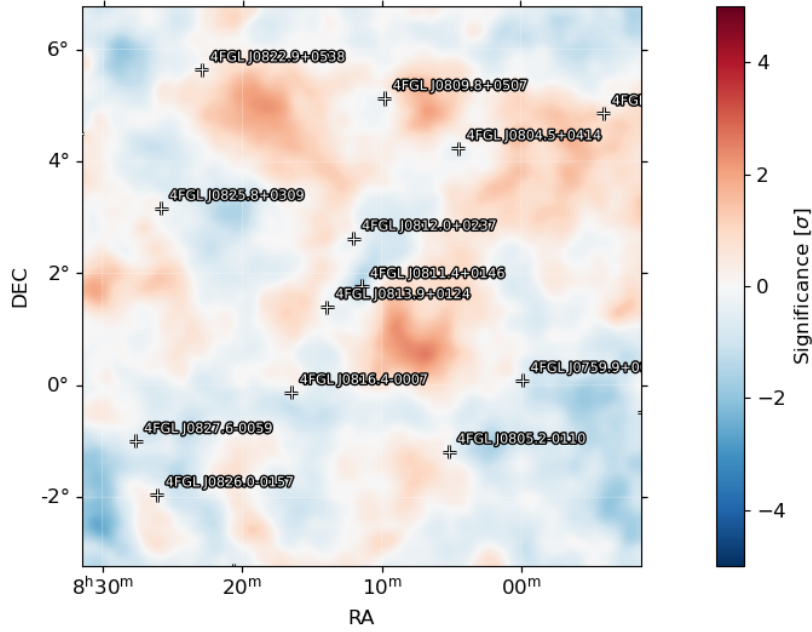


Figure 3: Residual map of OJ 014.

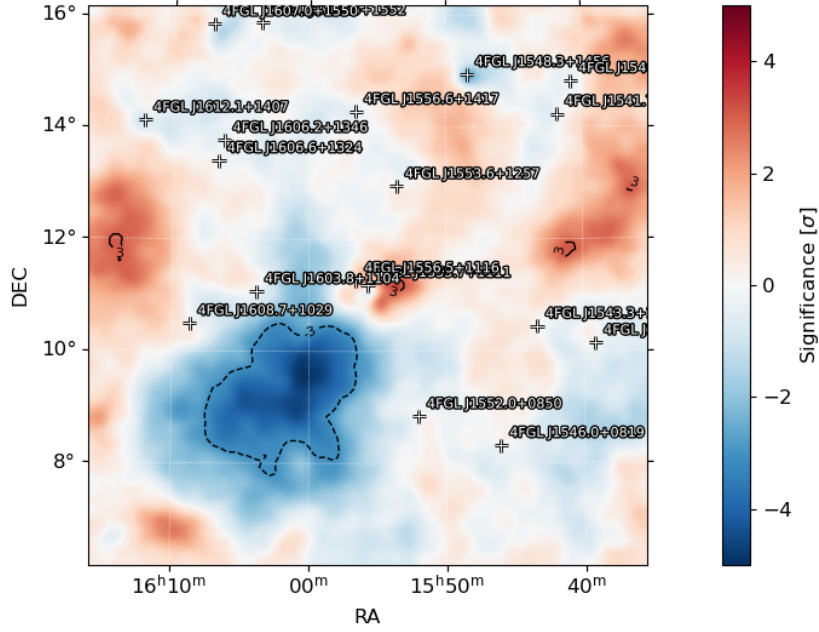


Figure 4: Residual map of PG 1553+113. The larger deviations in the bottom left and elsewhere hint at an insufficient background modelling coming from the given galdif and isodif background files. This region in the sky is already known and will be studied in the future.

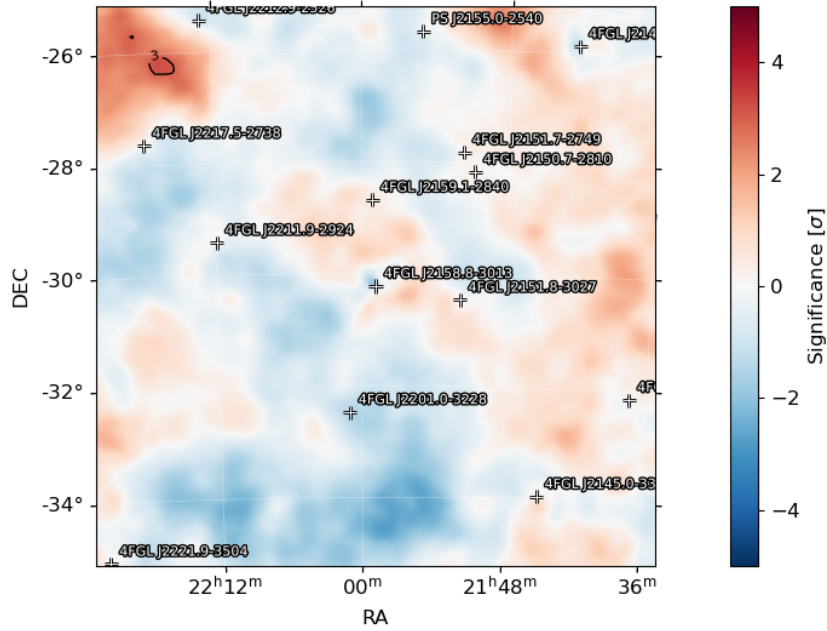


Figure 5: Residual map of PKS2155.

Final Spline Detrending and sine fitting

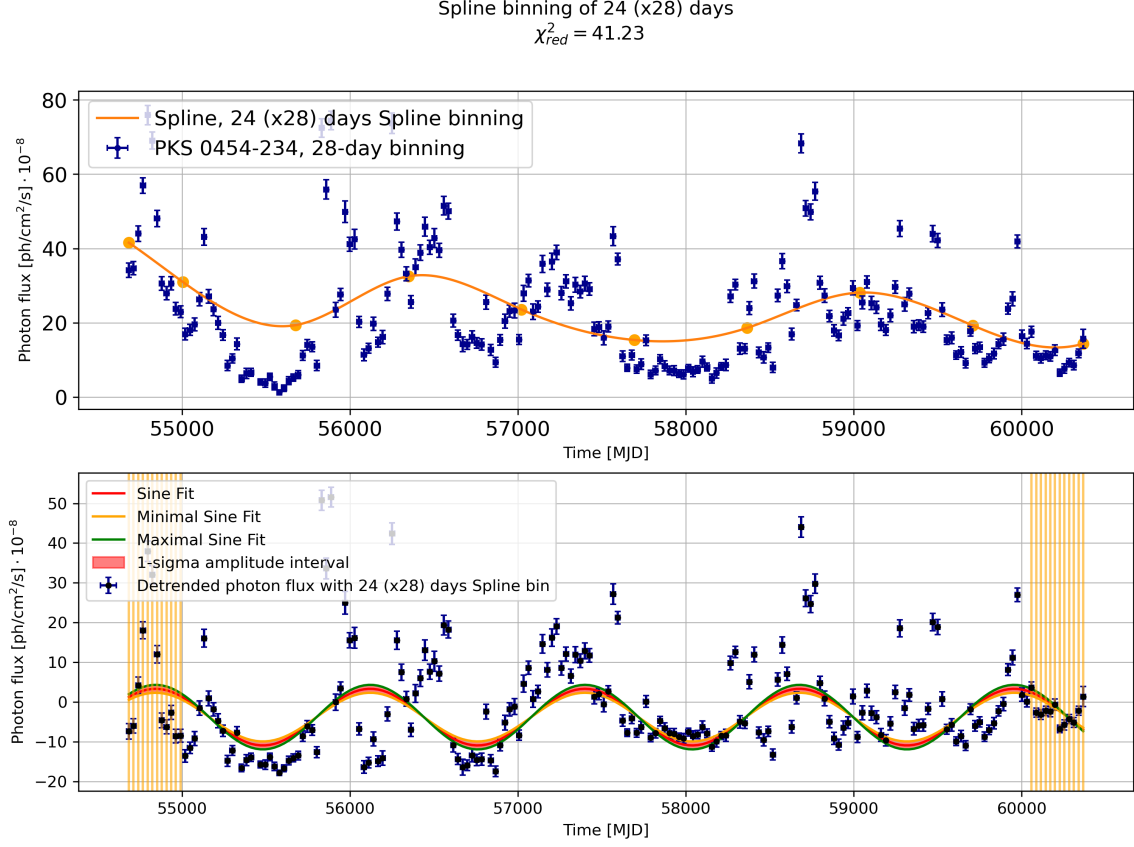


Figure 6: In this figure, the Spline detrending as well as the sine fitting is shown for PKS 0454-234. The best Spline as well as the original LC are plotted in the upper panel. For the Spline binning, the value determined in section 5.2.4 was used for the optimal detrending. In the lower panel, the detrended LC and the sine fit are shown. Furthermore, the 1- σ -band is plotted between the sinusoidal waves with amplitudes plus (minus) the error of the amplitude. The vertical bars at the edges of the time interval mark the excluded data points for the sine fit due to the endpoints of the Spline.

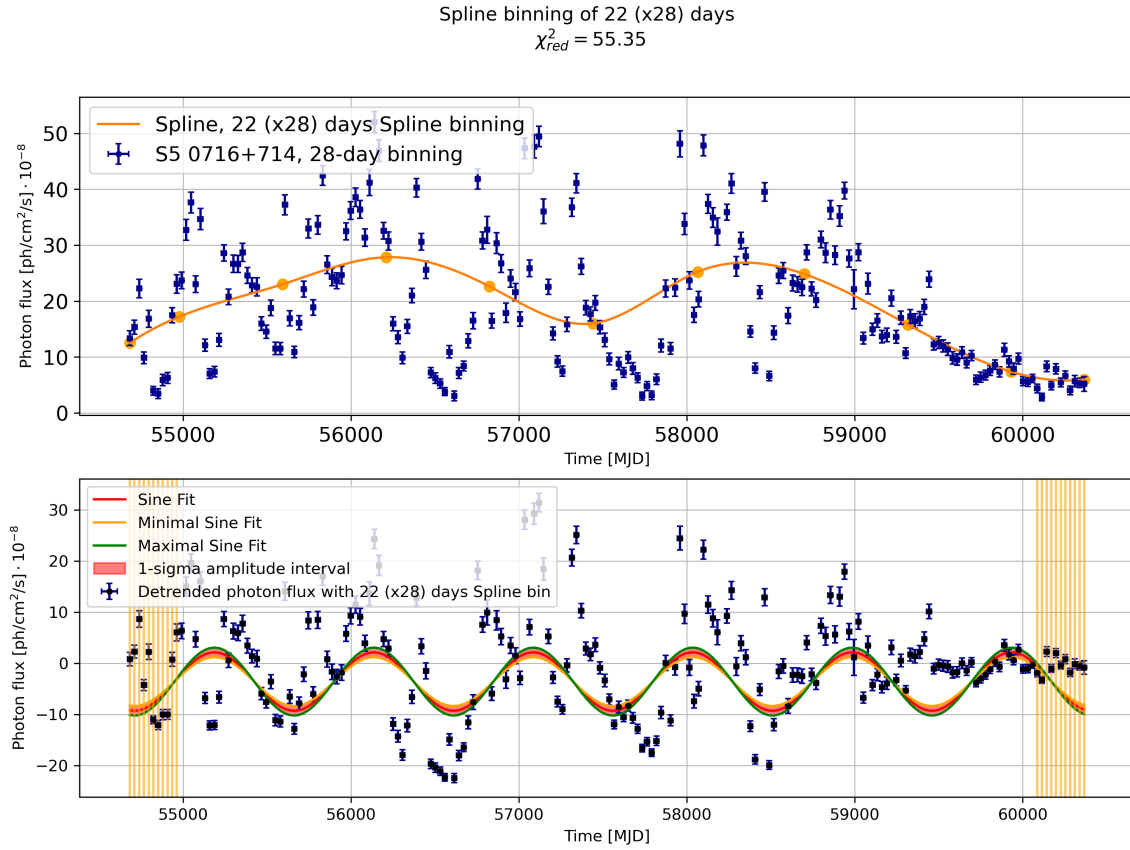


Figure 7: In this figure, the Spline detrending as well as the sine fitting is shown for S5 0716+714. The best Spline as well as the original LC are plotted in the upper panel. For the Spline binning, the value determined in section 5.2.4 was used for the optimal detrending. In the lower panel, the detrended LC and the sine fit are shown. Furthermore, the 1- σ -band is plotted between the sinusoidal waves with amplitudes plus (minus) the error of the amplitude. The vertical bars at the edges of the time interval mark the excluded data points for the sine fit due to the endpoints of the Spline.

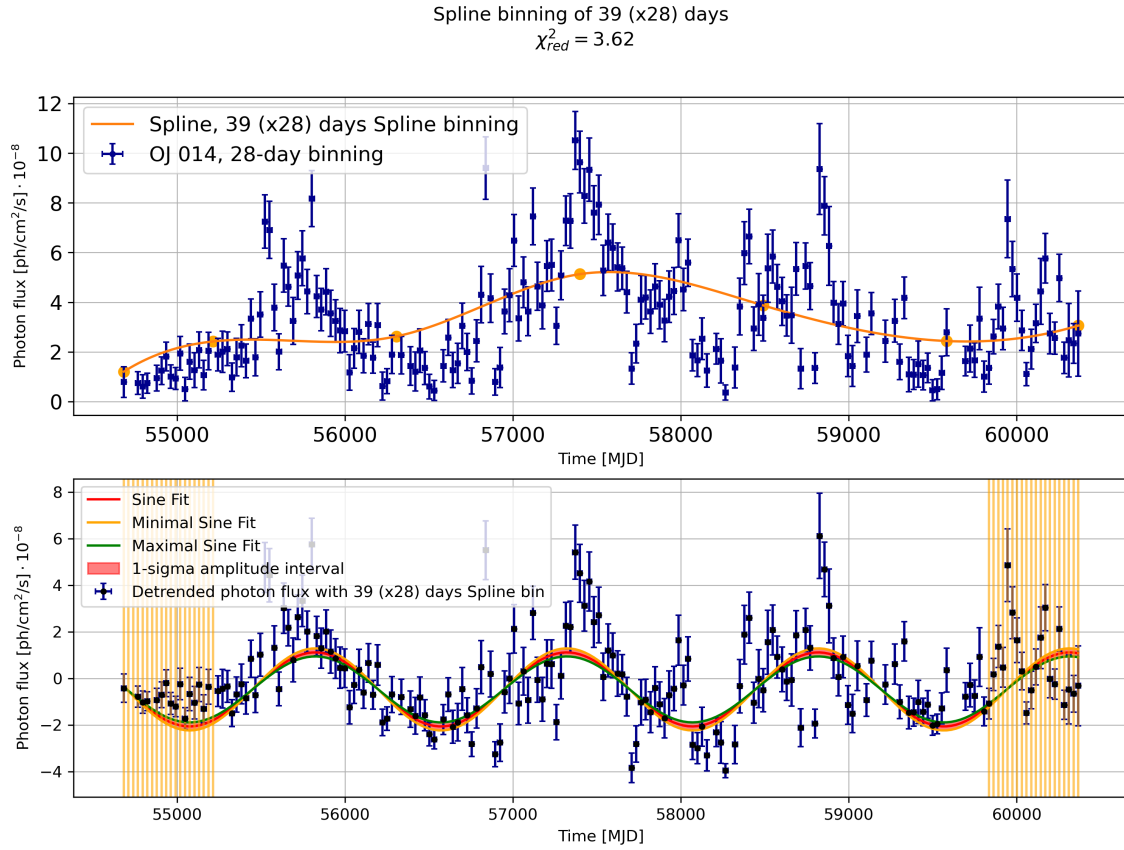


Figure 8: In this figure, the Spline detrending as well as the sine fitting is shown for OJ 014. The best Spline as well as the original LC are plotted in the upper panel. For the Spline binning, the value determined in section 5.2.4 was used for the optimal detrending. In the lower panel, the detrended LC and the sine fit are shown. Furthermore, the 1- σ -band is plotted between the sinusoidal waves with amplitudes plus (minus) the error of the amplitude. The vertical bars at the edges of the time interval mark the excluded data points for the sine fit due to the endpoints of the Spline.

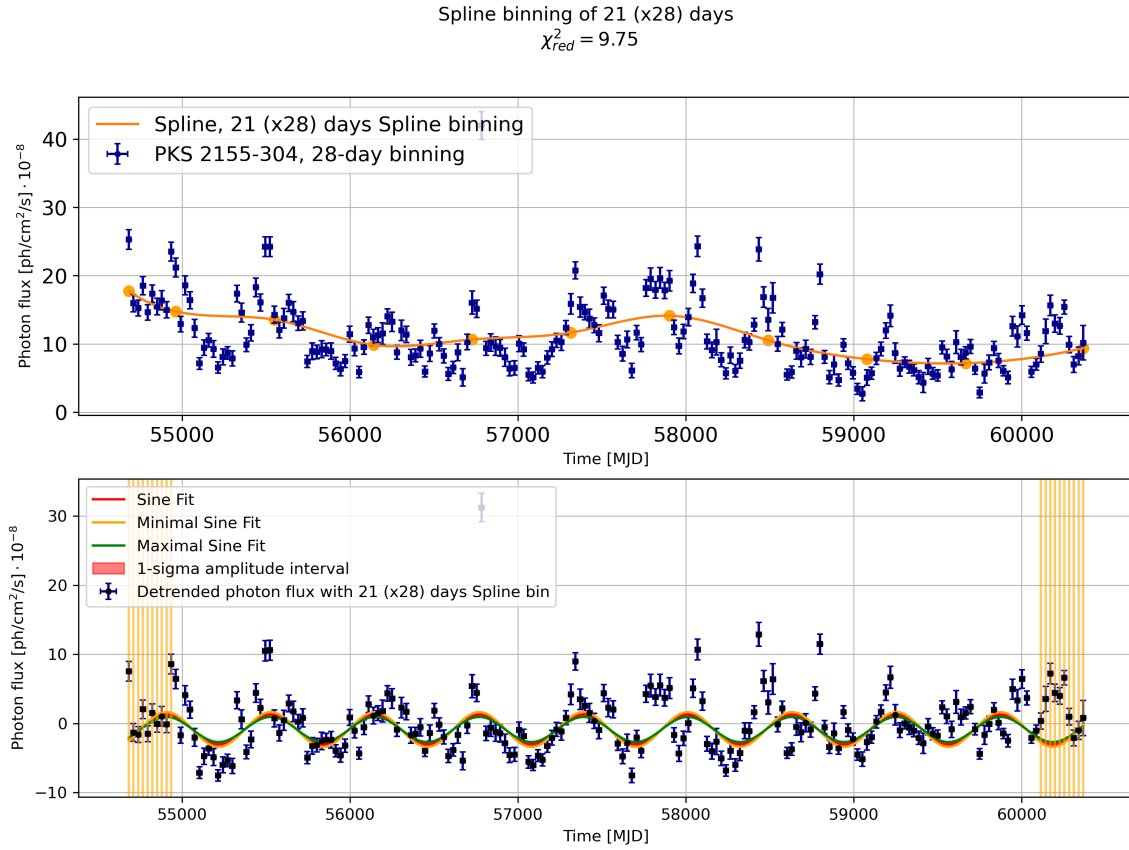


Figure 9: In this figure, the Spline detrending as well as the sine fitting is shown for PKS 2155-304. The best Spline as well as the original LC are plotted in the upper panel. For the Spline binning, the value determined in section 5.2.4 was used for the optimal detrending. In the lower panel, the detrended LC and the sine fit are shown. Furthermore, the 1- σ -band is plotted between the sinusoidal waves with amplitudes plus (minus) the error of the amplitude. The vertical bars at the edges of the time interval mark the excluded data points for the sine fit due to the endpoints of the Spline.

χ_{red}^2 and amplitude diagrams

PKS 0454-234

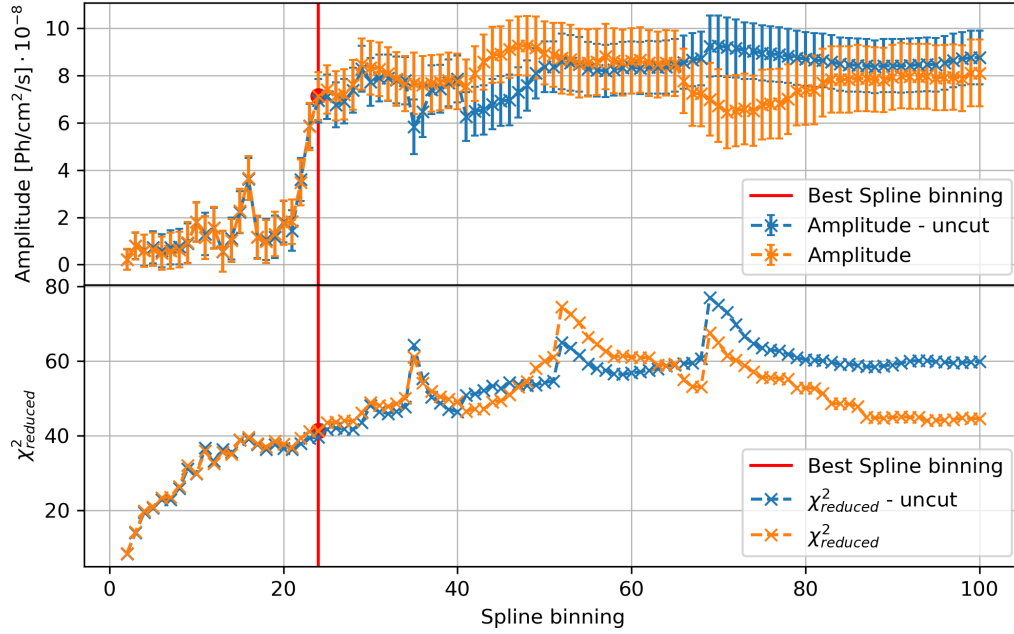


Figure 10: In the upper panel, the resulting amplitude from the sine fit is shown for the 2 – 100 tested Spline bins. In the lower panel, the corresponding χ_{red}^2 is shown. The orange line displays the amplitude fit with half a Spline bin excluded at both ends of the time interval. The blue line displays the amplitude fit on the full-time interval. The best Spline binning for the analysis with reduced time interval (stated in Table 5.5) is marked in red.

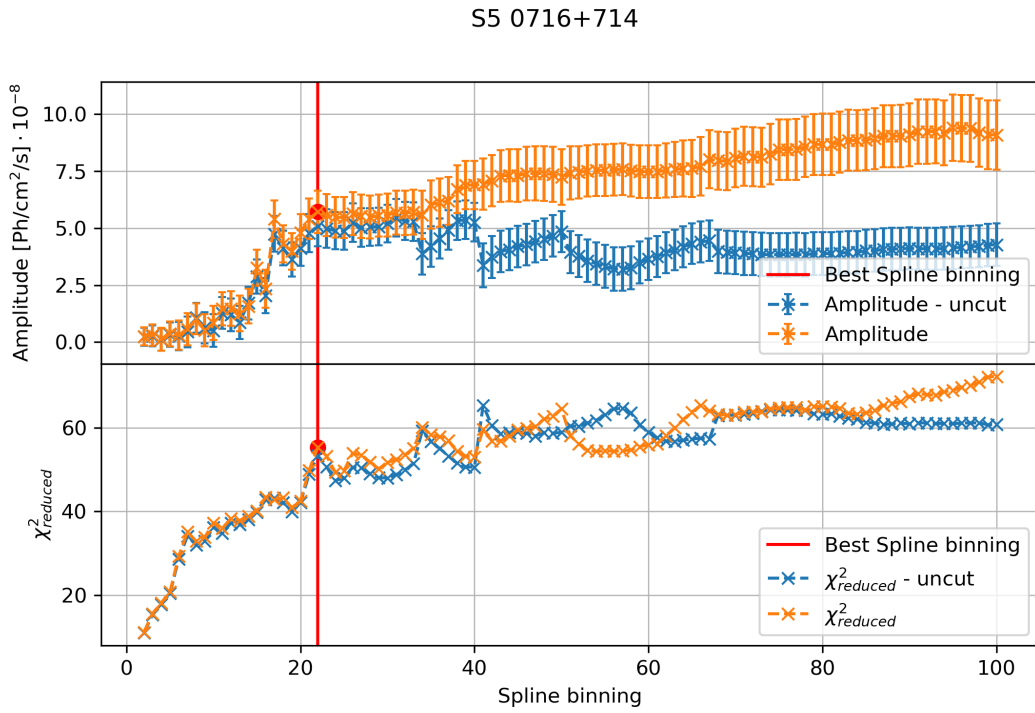


Figure 11: In the upper panel, the resulting amplitude from the sine fit is shown for the 2 – 100 tested Spline bins. In the lower panel, the corresponding χ^2_{red} is shown. The orange line displays the amplitude fit with half a Spline bin excluded at both ends of the time interval. The blue line displays the amplitude fit on the full-time interval. The best Spline binning for the analysis with reduced time interval (stated in Table 5.5) is marked in red.

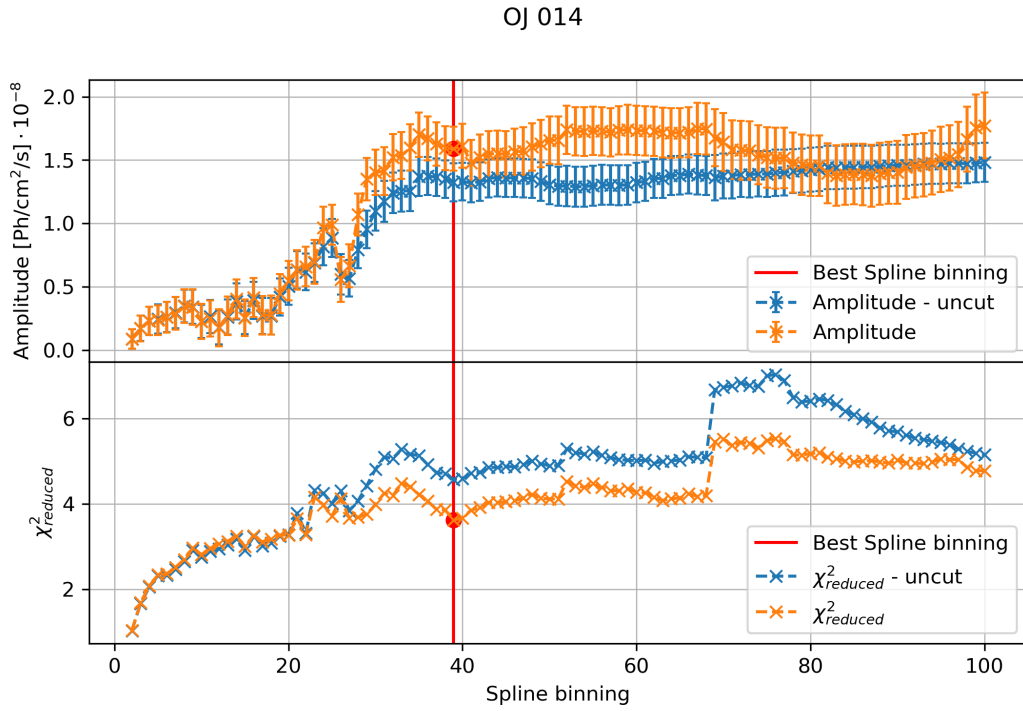


Figure 12: In the upper panel, the resulting amplitude from the sine fit is shown for the 2 – 100 tested Spline bins. In the lower panel, the corresponding χ^2_{red} is shown. The orange line displays the amplitude fit with half a Spline bin excluded at both ends of the time interval. The blue line displays the amplitude fit on the full-time interval. The best Spline binning for the analysis with reduced time interval (stated in Table 5.5) is marked in red.

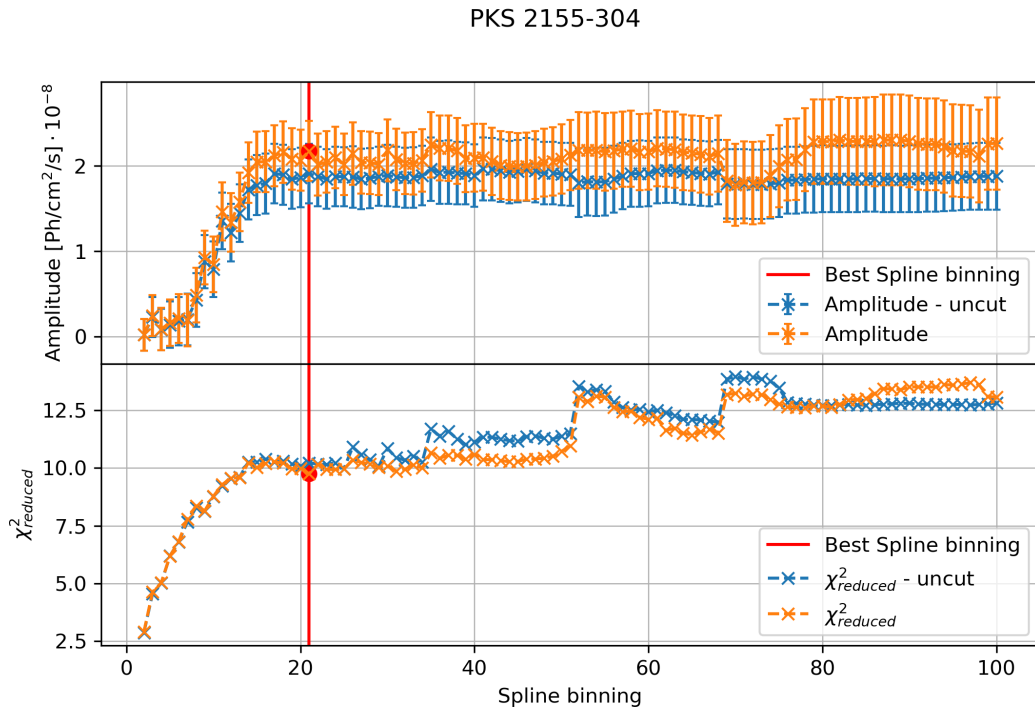


Figure 13: In the upper panel, the resulting amplitude from the sine fit is shown for the 2 – 100 tested Spline bins. In the lower panel, the corresponding χ^2_{red} is shown. The orange line displays the amplitude fit with half a Spline bin excluded at both ends of the time interval. The blue line displays the amplitude fit on the full-time interval. The best Spline binning for the analysis with reduced time interval (stated in Table 5.5) is marked in red.

Bibliography

- [1] Daniel J. D’Orazio and Maria Charisi. Observational Signatures of Supermassive Black Hole Binaries. *arXiv e-prints*, page arXiv:2310.16896, October 2023.
- [2] State Office for Heritage Management and Archaeology Saxony-Anhalt. Nebra Sky Disc. <https://www.landeshmuseum-vorgeschichte.de/en/nebra-sky-disc.html>, 2024.
- [3] A. Einstein. Sitzungsber. K. Preuss. Akad. Wiss. 1, 688. 1916.
- [4] A. Einstein. Sitzungsber. K. Preuss. Akad. Wiss. 1, 154. 1918.
- [5] B. P. Abbott, LIGO Scientific Collaboration, and Virgo Collaboration et al. Observation of Gravitational Waves from a Binary Black Hole Merger. *Physical Review Letters*, 116(6):061102, February 2016.
- [6] Gabriella Agazie et al. The NANOGrav 15 yr Data Set: Constraints on Supermassive Black Hole Binaries from the Gravitational-wave Background. *The Astrophysical Journal Letters*, 952(2):L37, August 2023.
- [7] EPTA Collaboration and J. Antoniadis et al. The second data release from the European Pulsar Timing Array IV. Search for continuous gravitational wave signals. *arXiv e-prints*, page arXiv:2306.16226, June 2023.
- [8] Toby Saunders. Number of galaxies estimate. <https://www.sciencefocus.com/space/how-many-galaxies-are-in-the-universe>, 2023.
- [9] Volker Beckmann and Chris R. Shrader. *Active Galactic Nuclei*. 2012.
- [10] P. Padovani, D. M. Alexander, R. J. Assef, B. De Marco, P. Giommi, R. C. Hickox, G. T. Richards, V. Smolčić, E. Hatziminaoglou, V. Mainieri, and M. Salvato. Active galactic nuclei: what’s in a name? *Astronomy and Astrophysics Reviews*, 25(1):2, August 2017.
- [11] C. Megan Urry and Paolo Padovani. Unified Schemes for Radio-Loud Active Galactic Nuclei. *Publications of the ASP*, 107:803, September 1995.

- [12] Jessica E. Thorne, Aaron S. G. Robotham, Luke J. M. Davies, Sabine Bellstedt, Michael J. I. Brown, Scott M. Croom, Ivan Delvecchio, Brent Groves, Matt J. Jarvis, Stanislav S. Shabala, Nick Seymour, Imogen H. Whittam, Matias Bravo, Robin H. W. Cook, Simon P. Driver, Benne Holwerda, Steven Phillipps, and Malgorzata Siudek. Deep Extragalactic VISIBLE Legacy Survey (DEVILS): identification of AGN through SED fitting and the evolution of the bolometric AGN luminosity function. *Monthly Notices of the RAS*, 509(4):4940–4961, February 2022.
- [13] Jessica E. Thorne, Aaron S. G. Robotham, Luke J. M. Davies, and Sabine Bellstedt. AGN Unification Diagram. <https://doi.org/10.5281/zenodo.6381013>, 2022.
- [14] M. Ackermann, et al. The Spectrum of Isotropic Diffuse Gamma-Ray Emission between 100 MeV and 820 GeV. *Astrophysical Journal*, 799(1):86, January 2015.
- [15] C. M. Raiteri, M. Villata, and J. A. Acosta-Pulido et al. Blazar spectral variability as explained by a twisted inhomogeneous jet. *Nature*, 552(7685):374–377, December 2017.
- [16] P. Peñil, M. Ajello, S. Buson, A. Domínguez, J. R. Westernacher-Schneider, and J. Zrake. Evidence of Periodic Variability in Gamma-ray Emitting Blazars with Fermi-LAT. *arXiv e-prints*, page arXiv:2211.01894, November 2022.
- [17] Marc Postman et al. The Cluster Lensing and Supernova Survey with Hubble: An Overview. *Astrophysical Journal, Supplement*, 199(2):25, April 2012.
- [18] Margherita De Toma. *Study of temporal patterns in the gravitational lensed blazar PKS 1830-211 with the Fermi Large Area Telescope*. Theses, University of Pisa, 2022.
- [19] J. Gracia, J. Peitz, Ch. Keller, and M. Camenzind. Evolution of bimodal accretion flows. *Monthly Notices of the Royal Astronomical Society*, 344(2):468–472, September 2003.
- [20] M. Tavani, A. Cavaliere, Pere Munar-Adrover, and A. Argan. The Blazar PG 1553+113 as a Binary System of Supermassive Black Holes. *Astrophysical Journal*, 854(1):11, February 2018.
- [21] Frank M. Rieger. On the Geometrical Origin of Periodicity in Blazar-type Sources. *Astrophysical Journal, Letters*, 615(1):L5–L8, November 2004.
- [22] Marco Celoria, Roberto Oliveri, Alberto Sesana, and Michela Mapelli. Lecture notes on black hole binary astrophysics. *arXiv e-prints*, page arXiv:1807.11489, July 2018.
- [23] Frank M. Rieger. Supermassive binary black holes among cosmic gamma-ray sources. *Astrophysics and Space Science*, 309(1-4):271–275, June 2007.

- [24] Miguel Preto, Ingo Berentzen, Peter Berczik, and Rainer Spurzem. Fast Coalescence of Massive Black Hole Binaries from Mergers of Galactic Nuclei: Implications for Low-frequency Gravitational-wave Astrophysics. *Astrophysical Journal, Letters*, 732(2):L26, May 2011.
- [25] Joshua E. Barnes. Formation of gas discs in merging galaxies. *Monthly Notices of the RAS*, 333(3):481–494, July 2002.
- [26] Taeho Ryu, Rosalba Perna, Zoltán Haiman, Jeremiah P. Ostriker, and Nicholas C. Stone. Interactions between multiple supermassive black holes in galactic nuclei: a solution to the final parsec problem. *Monthly Notices of the RAS*, 473(3):3410–3433, January 2018.
- [27] Matteo Bonetti, Alberto Sesana, Francesco Haardt, Enrico Barausse, and Monica Colpi. Post-Newtonian evolution of massive black hole triplets in galactic nuclei - IV. Implications for LISA. *Monthly Notices of the RAS*, 486(3):4044–4060, July 2019.
- [28] Elisa Bortolas, Michela Mapelli, and Mario Spera. Star cluster disruption by a massive black hole binary. *Monthly Notices of the RAS*, 474(1):1054–1064, February 2018.
- [29] Hagai B. Perets, Clovis Hopman, and Tal Alexander. Massive Perturber-driven Interactions between Stars and a Massive Black Hole. *Astrophysical Journal*, 656(2):709–720, February 2007.
- [30] F. Müller-Sánchez, J. M. Comerford, R. Nevin, R. S. Barrows, M. C. Cooper, and J. E. Greene. The Origin of Double-peaked Narrow Lines in Active Galactic Nuclei. I. Very Large Array Detections of Dual AGNs and AGN Outflows. *Astrophysical Journal*, 813(2):103, November 2015.
- [31] Alessandra De Rosa, et al. The quest for dual and binary supermassive black holes: A multi-messenger view. *New Astronomy Review*, 86:101525, December 2019.
- [32] George B. Rybicki and Alan P. Lightman. *Radiative Processes in Astrophysics*. 1986.
- [33] Matteo Cerruti. Leptonic and Hadronic Radiative Processes in Supermassive-Black-Hole Jets. *Galaxies*, 8(4):72, October 2020.
- [34] Maria Charisi, Stephen R. Taylor, Jessie Runnoe, Tamara Bogdanovic, and Jonathan R. Trump. Multimessenger time-domain signatures of supermassive black hole binaries. *Monthly Notices of the RAS*, 510(4):5929–5944, March 2022.
- [35] W. B. Atwood, et al. The Large Area Telescope on the Fermi Gamma-Ray Space Telescope Mission. *Astrophysical Journal*, 697(2):1071–1102, June 2009.

- [36] ENRICO Fermi. On the origin of the cosmic radiation. *Phys. Rev.*, 75:1169–1174, Apr 1949.
- [37] R. P. Johnson and R. Mukherjee. GeV telescopes: results and prospects for Fermi. *New Journal of Physics*, 11(5):055008, May 2009.
- [38] FSSC. Spectral models. https://fermi.gsfc.nasa.gov/ssc/data/analysis/scitools/source_models.html#LogParabola, 2023.
- [39] H. Cramer. *Science* 104. 1946.
- [40] R. C. Rao. *Bull. Calcutta Math. Soc.* 37, 81. 1945.
- [41] Fermipy documentation. <https://fermipy.readthedocs.io/en/latest/advanced/residmap.html>, 2024.
- [42] FSSC. Fermitools documentation. <https://fermi.gsfc.nasa.gov/ssc/data/analysis/documentation/Cicerone/>, 2024.
- [43] Hubing Xiao, Zhihao Ouyang, Lixia Zhang, Liping Fu, Shaohua Zhang, Xiangtao Zeng, and Junhui Fan. The Relativistic Jet and Central Engine of Fermi Blazars. *Astrophysical Journal*, 925(1):40, January 2022.
- [44] J.R. Taylor. *Fehleranalyse: eine Einführung in die Untersuchung von Unsicherheiten in physikalischen Messungen*. VCH, 1988.
- [45] Yue Shen, Jenny E. Greene, Michael A. Strauss, Gordon T. Richards, and Donald P. Schneider. Biases in Virial Black Hole Masses: An SDSS Perspective. *Astrophysical Journal*, 680(1):169–190, June 2008.
- [46] Yong-gang Zheng, Wei-guo Yang, Hao-jing Zhang, and Xiong Zhang. Characteristics of the Radiation from Blazars. *Chinese Astronomy and Astrophysics*, 32(2):140–150, April 2008.
- [47] Yutong Chen, Tingfeng Yi, Junping Chen, He Lu, Yuncai Shen, Junjie Wang, Liang Wang, Shun Zhang, Lisheng Mao, and Liang Dong. Revisiting the quasi-periodic oscillations in blazar PG 1553+113 with multi-wavebands data. *New Astronomy*, 108:102186, May 2024.
- [48] Yongyun Chen, Qiusheng Gu, Junhui Fan, Xiaoling Yu, Xiaogu Zhong, Hongyu Liu, Nan Ding, Dingrong Xiong, and Xiaotong Guo. General Physical Properties of Fermi Blazars. *Astrophysical Journal, Supplement*, 268(1):6, September 2023.

- [49] J. Ballet, P. Bruel, T. H. Burnett, B. Lott, and The Fermi-LAT collaboration. Fermi Large Area Telescope Fourth Source Catalog Data Release 4 (4FGL-DR4). *arXiv e-prints*, page arXiv:2307.12546, July 2023.
- [50] M. Zechmeister and M. Kürster. The generalised Lomb-Scargle periodogram. A new formalism for the floating-mean and Keplerian periodograms. *Astronomy and Astrophysics*, 496(2):577–584, March 2009.
- [51] S. Mishra, H. Chand, Gopal Krishna, R. Joshi, Y. A. Shchekinov, and T. A. Fatkhullin. On the incidence of Mg II absorbers along the blazar sightlines. *Monthly Notices of the RAS*, 473(4):5154–5164, February 2018.
- [52] J. Dorigo Jones, S. D. Johnson, Sowgat Muzahid, J. Charlton, H. W. Chen, A. Narayanan, Sameer, J. Schaye, and N. A. Wijers. Improving blazar redshift constraints with the edge of the Ly α forest: 1ES 1553+113 and implications for observations of the WHIM. *Monthly Notices of the RAS*, 509(3):4330–4343, January 2022.
- [53] Marco Landoni, R. Falomo, S. Paiano, and A. Treves. ZBLLAC: A Spectroscopic Database of BL Lacertae Objects. *Astrophysical Journal, Supplement*, 250(2):37, October 2020.
- [54] Marcel Neeleman, J. Xavier Prochaska, Joseph Ribaudo, Nicolas Lehner, J. Christopher Howk, Marc Rafelski, and Nissim Kanekar. The H I Content of the Universe Over the Past 10 GYRS. *The Astrophysical Journal*, 818(2):113, February 2016.
- [55] R. Falomo, Joseph E. Pesce, and A. Treves. The Environment of the BL Lacertae Object PKS 2155-304. *Astrophysical Journal Letters*, 411:L63, July 1993.
- [56] W. F. Welsh. On the Reliability of Cross-Correlation Function Lag Determinations in Active Galactic Nuclei. *Publications of the ASP*, 111(765):1347–1366, November 1999.
- [57] Pauli Virtanen, Ralf Gommers, Travis E. Oliphant, Matt Haberland, Tyler Reddy, David Cournapeau, Evgeni Burovski, Pearu Peterson, Warren Weckesser, Jonathan Bright, Stéfan J. van der Walt, Matthew Brett, Joshua Wilson, K. Jarrod Millman, Nikolay Mayorov, Andrew R. J. Nelson, Eric Jones, Robert Kern, Eric Larson, C J Carey, İlhan Polat, Yu Feng, Eric W. Moore, Jake VanderPlas, Denis Laxalde, Josef Perktold, Robert Cimrman, Ian Henriksen, E. A. Quintero, Charles R. Harris, Anne M. Archibald, Antônio H. Ribeiro, Fabian Pedregosa, Paul van Mulbregt, and SciPy 1.0 Contributors. SciPy 1.0: Fundamental Algorithms for Scientific Computing in Python. *Nature Methods*, 17:261–272, 2020.

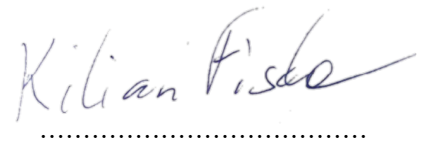
-
- [58] Maria Charisi, Zoltán Haiman, David Schiminovich, and Daniel J. D’Orazio. Testing the relativistic Doppler boost hypothesis for supermassive black hole binary candidates. *Monthly Notices of the RAS*, 476(4):4617–4628, June 2018.
- [59] Frank M. Rieger. Supermassive binary black holes in blazars. In E. J. A. Meurs and G. Fabbiano, editors, *Populations of High Energy Sources in Galaxies*, volume 230, pages 239–240, January 2006.
- [60] S. O’Neill et al. The Unanticipated Phenomenology of the Blazar PKS 2131-021: A Unique Supermassive Black Hole Binary Candidate. *Astrophysical Journal, Letters*, 926(2):L35, February 2022.
- [61] H. Abe et al. The variability patterns of the TeV blazar PG 1553 + 113 from a decade of MAGIC and multiband observations. *Monthly Notices of the RAS*, 529(4):3894–3911, April 2024.

Declaration of originality

I declare that I have authored this thesis independently, that I have not used other than the declared sources / resources, and that I have explicitly marked all material which has been quoted either literally or by content from the used sources. I hereby also declare, that my Thesis has not been prepared for another examination or assignment, either wholly or excerpts thereof.

Hiermit erkläre ich, dass ich der alleinige Autor dieser Arbeit bin und keine anderen Quellen oder Hilfen, außer den aufgeführten, verwendet wurden. Weiterhin erkläre ich, dass ich die Arbeit Anderer durch detaillierte Referenzen anerkannt habe. Ebenso erkläre ich hiermit, dass meine Arbeit nicht für eine andere Prüfung oder Aufgabe, weder vollständig noch in Auszügen, vorbereitet wurde.

Würzburg, 05.05.2024

A handwritten signature in blue ink that reads "Kilian Fiske". The signature is written in a cursive style with a long, sweeping underline.

.....
Signature